

AN ENTROPY-STABLE OSCILLATION-ELIMINATING DGSEM FOR THE EULER EQUATIONS ON CURVILINEAR MESHES

JIELING YANG¹ AND GUOSHENG FU¹

ABSTRACT. We develop an entropy-stable high-order numerical method for the two-dimensional compressible Euler equations on general curvilinear meshes. The proposed approach is based on a nodal discontinuous Galerkin spectral element method (DGSEM) that satisfies the summation-by-parts (SBP) property. At the semidiscrete level, entropy stability is established through the SBP structure and the discrete metric identities associated with curvilinear coordinate mappings. By incorporating entropy-stable numerical fluxes at element interfaces, a global discrete entropy inequality is obtained. To further control nonphysical oscillations near strong discontinuities, the entropy-stable DG formulation is combined with a modified oscillation-eliminating discontinuous Galerkin (OEDG) method, which was originally proposed in [59]. We observe that the zero-order damping coefficient in the original OEDG method naturally serves as an effective shock indicator, which enables localization of the oscillation control mechanism and significantly reduces computational cost. Moreover, while the original OEDG formulation relies on local orthogonal modal bases and is primarily restricted to simplicial meshes, we reformulate the OE procedure using projection operators, allowing for a systematic extension to general curvilinear meshes. The resulting method preserves conservation and entropy stability while effectively suppressing spurious oscillations. A series of challenging numerical experiments is presented to demonstrate the accuracy, robustness, and effectiveness of the proposed entropy-stable OEDG method on both Cartesian and curvilinear meshes.

Keywords: *Euler equation, discontinuous Galerkin method, curvilinear mesh, entropy stable, oscillation eliminating, shock indicator*

1. INTRODUCTION

The compressible Euler equations play a fundamental role in fluid dynamics and serve as a core mathematical model for a wide range of applications, including aerodynamics, astrophysical flows, gas dynamics, and high-speed compressible flows. As a nonlinear hyperbolic system of conservation laws, the Euler equations admit complex solution structures such as shock waves, contact discontinuities, and rarefaction waves, even when evolving from smooth initial data. Accurately and robustly resolving these multiscale and strongly nonlinear phenomena remains a central challenge in computational fluid dynamics [2, 1].

The development of numerical methods for the Euler equations is driven by the simultaneous requirements of accuracy, stability, and robustness. Among the many numerical approaches that have been proposed, discontinuous Galerkin (DG) methods are particularly attractive due to their ability to achieve high-order accuracy on complex geometries while maintaining local conservation. Consequently, DG methods have become an increasingly popular choice for the approximation of hyperbolic conservation laws, including the compressible Euler equations [18]. Beyond accuracy, stability and robustness are essential for reliable simulations. In particular, preserving fundamental physical properties of the Euler equations, such as entropy stability and positivity of density and pressure, is crucial for the success of a numerical scheme. In addition, the control of nonphysical numerical oscillations near discontinuities remains an important and challenging issue for high-order methods.

The entropy inequality is a fundamental physical property of the Euler equations and serves as an admissibility criterion for physically relevant solutions. It is well known that shock waves and contact discontinuities may develop during the evolution of the Euler equations, even when the initial and boundary data are smooth. As a consequence, solutions are generally understood in the weak (distributional) sense. However, weak solutions are not unique, and additional

This work is supported in part by NSF DMS-2410740.

admissibility conditions are required to single out the physically meaningful solution. This role is played by entropy conditions, which are consistent with the second law of thermodynamics. From a numerical perspective, it is therefore essential to design schemes that preserve entropy properties at the discrete level. The pioneering work of Tadmor [68] introduced the concept of entropy-conservative and entropy-stable schemes for systems of conservation laws, leading to the construction of first-order entropy-stable finite volume methods based on specially designed entropy-conservative numerical fluxes. Subsequent extensions include second-order schemes [69] and arbitrarily high-order methods [27], relying on high-order entropy-conservative flux constructions [50]. These developments laid the theoretical foundation for entropy-stable high-order discretizations.

In the context of discontinuous Galerkin (DG) methods, early progress on entropy stability was made by Jiang and Shu [45], who established a discrete entropy inequality for scalar conservation laws using the square entropy. This analysis was later extended to linear symmetric hyperbolic systems by Hou and LeFloch [40]. Despite these foundational contributions, entropy-stable DG formulations remained limited in both scope and applicability for many years. Substantial advances have been achieved more recently through the work of Carpenter et al. [8, 24], who exploited the summation-by-parts (SBP) property of nodal DG discretizations based on Gauss–Legendre–Lobatto (GLL) points. These methods are commonly referred to as the DG spectral element method with Gauss–Legendre–Lobatto points (DGSEM–GLL) [20, 76]. Building on this framework, Chen and Shu [14, 15] developed a unified approach for constructing high-order entropy-stable DG methods for general systems on unstructured triangular meshes using SBP operators. Further developments and refinements of entropy-stable DGSEM formulations have been reported in [19, 10, 11]. Entropy-stable DGSEM–GLL methods have since been successfully applied to a broad class of systems, including the Euler and Navier–Stokes equations [19], shallow water equations [32, 73], magnetohydrodynamics (MHD) [6, 55], and multiphase or multicomponent flows [64]. Finally, it is worth noting that DGSEM–GLL methods are closely related to summation-by-parts finite difference operators coupled with simultaneous approximation terms (SAT) [31, 30].

The construction of entropy-stable schemes on curvilinear meshes poses additional challenges. In this setting, entropy stability must be achieved simultaneously with the preservation of discrete geometric conservation laws (GCLs), which is essential for maintaining free-stream preservation and nonlinear stability. Important progress in this direction has been reported in [26, 9, 19, 12, 6], where careful discretization of geometric terms is required to ensure compatibility between entropy stability and the discrete metric identities [46].

Despite these advances, entropy stability alone is generally insufficient to eliminate nonphysical oscillations near strong discontinuities. Such oscillations are closely related to the classical Gibbs phenomenon [34] and are particularly pronounced in high-order numerical schemes, including discontinuous Galerkin methods. If left uncontrolled, Gibbs-type oscillations may severely degrade solution quality, compromise robustness, or even lead to numerical breakdown. Consequently, additional nonlinear stabilization mechanisms are indispensable in practical computations for hyperbolic conservation laws. A wide range of shock-capturing techniques has been developed to suppress nonphysical oscillations. Limiter-based approaches, such as total variation diminishing (TVD) and total variation bounded (TVB) limiters [18, 7], as well as ENO and weighted ENO (WENO) limiters [62, 79, 80], modify local solution reconstructions in troubled cells to enforce monotonicity or boundedness. Another widely used strategy is the introduction of artificial viscosity (AV), which adds localized dissipation in regions with strong gradients [44, 43, 60, 5].

More recently, the oscillation-free DG (OFDG) framework has been systematically developed by Lu, Liu, and Shu [57, 53]. In OFDG, damping terms are incorporated directly into the DG formulation to suppress spurious oscillations. This approach has demonstrated strong robustness and has been extended to a variety of systems, including chemically reacting flows [23, 81], shallow water equations [56], and magnetohydrodynamics [54]. However, the additional damping terms render the resulting semidiscrete system highly stiff, leading to severe time-step restrictions in explicit time integration. To alleviate this limitation, Peng et al. proposed

the oscillation-eliminating DG (OEDG) method in [59]. The OEDG method follows a similar damping-based philosophy as OFDG, but formulates the oscillation control mechanism as a local pseudo-time evolution problem that can be solved exactly. As a result, the stiffness associated with the damping terms is removed, and the stringent time-step constraints of OFDG are largely mitigated. Since its introduction, OEDG has been successfully applied to a variety of problems, including systems with complex wave interactions [52, 22, 75].

Despite its advantages, the original OEDG formulation still faces several practical challenges. In particular, the computation of damping coefficients involves the evaluation of high-order spatial derivatives in multiple directions, which can be computationally expensive. Moreover, the direct extension of OEDG to curvilinear meshes is not straightforward due to the lack of tensor-product structure and the presence of geometric complexities. In this work, we address these limitations and further develop the OEDG framework. First, we observe that the damping coefficients appearing in the OE procedure naturally serve as effective shock indicators, closely related to the classical KXRCF indicator [47]. By exploiting this connection, the OE procedure can be selectively applied only in troubled cells, significantly reducing computational cost. Second, we extend the OEDG methodology to curvilinear meshes in a systematic and efficient manner.

The primary contribution of this work is the further development of the entropy stable oscillation-eliminating discontinuous Galerkin (OEDG) framework for the compressible Euler equations. Specifically, the OEDG methodology is generalized to curvilinear meshes, where geometric complexity poses additional challenges. A new shock indicator, derived directly from the OE damping coefficients, is introduced to localize the oscillation control mechanism and significantly reduce computational cost. The modified OEDG procedure is then combined with an entropy-stable DG formulation, resulting in a robust high-order nodal DG method that simultaneously enforces entropy stability and effectively suppresses nonphysical oscillations on general curvilinear meshes. The performance of the proposed method is demonstrated through a series of challenging numerical experiments.

The remainder of the paper is organized as follows. In Section 2, we review the entropy properties of the Euler equations, their formulation in curvilinear coordinates, and the nodal DG polynomial framework. Section 3 presents the entropy-stable DGSEM formulation on curvilinear meshes. The oscillation-eliminating procedure is introduced and analyzed in Section 4. Numerical examples demonstrating the accuracy, robustness, and effectiveness of the proposed method are provided in Section 5. Finally, concluding remarks are given in Section 6.

2. PRELIMINARY

This section summarizes the theoretical background required for the construction and analysis of entropy-stable nodal discontinuous Galerkin methods for the two-dimensional Euler equations on curvilinear meshes. In particular, we review the entropy properties of the Euler equations, introduce their formulation in curvilinear coordinates, and describe the nodal discontinuous Galerkin polynomial spaces used throughout this work.

2.1. Entropy properties of the Euler equations. We consider the compressible Euler equations written in conservative form

$$(1) \quad \partial_t \mathbf{U} + \nabla \cdot \mathbf{F}(\mathbf{U}) = 0,$$

where the vector of conservative variables is

$$(2) \quad \mathbf{U} = \begin{pmatrix} \rho \\ \rho \mathbf{u} \\ E \end{pmatrix},$$

with density ρ , velocity $\mathbf{u} = (u, v)^T$, and total energy

$$E = \rho e + \frac{1}{2} \rho |\mathbf{u}|^2.$$

The flux tensor is given by

$$(3) \quad \mathbf{F}(\mathbf{U}) = \begin{pmatrix} \rho \mathbf{u} \\ \rho \mathbf{u} \otimes \mathbf{u} + p \mathbf{I} \\ (E + p) \mathbf{u} \end{pmatrix},$$

where the pressure p is related to (ρ, e) through an equation of state. Throughout this work, we assume an ideal gas equation of state,

$$p = (\gamma - 1)\rho e, \quad \gamma = 1.4.$$

In two spatial dimensions, the flux tensor can be written as

$$(4) \quad \begin{aligned} \mathbf{F}(\mathbf{U}) &= (\mathbf{f}(\mathbf{U}), \mathbf{g}(\mathbf{U}))^T, \quad \mathbf{U} = (U_1, U_2, U_3, U_4)^T, \\ \mathbf{f}(\mathbf{U}) &= (\rho u, \rho u^2 + p, \rho u v, (E + p)u)^T, \\ \mathbf{g}(\mathbf{U}) &= (\rho v, \rho u v, \rho v^2 + p, (E + p)v)^T, \end{aligned}$$

so that the Euler equations take the componentwise form

$$(5) \quad \partial_t U_k + \partial_x f_k(\mathbf{U}) + \partial_y g_k(\mathbf{U}) = 0, \quad k = 1, \dots, 4.$$

The Euler system is nonlinear and hyperbolic, and solutions may develop discontinuities such as shocks and contact discontinuities in finite time, even for smooth initial data. As a consequence, weak solutions are generally not unique, and additional admissibility criteria are required to select physically relevant solutions. These criteria are provided by entropy conditions.

An *entropy function–entropy flux pair* $(\eta(\mathbf{U}), \mathbf{q}(\mathbf{U}))$ consists of a strictly convex scalar entropy η and an associated entropy flux \mathbf{q} satisfying

$$(6) \quad \eta'(\mathbf{U}) \mathbf{F}'(\mathbf{U}) = \mathbf{q}'(\mathbf{U}).$$

For smooth solutions, multiplication of the Euler equations by $\eta'(\mathbf{U})$ yields the entropy conservation law

$$(7) \quad \partial_t \eta(\mathbf{U}) + \nabla \cdot \mathbf{q}(\mathbf{U}) = 0.$$

Across discontinuities, entropy is no longer conserved. A weak solution \mathbf{U} is called an *entropy solution* if it satisfies the entropy inequality

$$(8) \quad \partial_t \eta(\mathbf{U}) + \nabla \cdot \mathbf{q}(\mathbf{U}) \leq 0 \quad \text{in the sense of distributions,}$$

which is consistent with the second law of thermodynamics.

Associated with a convex entropy $\eta(\mathbf{U})$ are the *entropy variables*

$$(9) \quad \mathbf{V} := \frac{\partial \eta}{\partial \mathbf{U}}.$$

Strict convexity of η implies that the mapping $\mathbf{U} \leftrightarrow \mathbf{V}$ is one-to-one on the admissible state space. Introducing the flux functions expressed in entropy variables, $\mathbf{G}(\mathbf{V}) = \mathbf{F}(\mathbf{U}(\mathbf{V}))$, the compatibility condition above is equivalent to the symmetry of the Jacobians $\mathbf{G}'_j(\mathbf{V})$ for each spatial direction j . This symmetrization property is fundamental for entropy analysis and motivates the introduction of the potential function and potential fluxes,

$$(10) \quad \begin{aligned} \phi(\mathbf{V}) &= \mathbf{U}(\mathbf{V})^T \mathbf{V} - \eta(\mathbf{U}(\mathbf{V})), \\ \psi_j(\mathbf{V}) &= \mathbf{G}_j(\mathbf{V})^T \mathbf{V} - \mathbf{q}_j(\mathbf{U}(\mathbf{V})), \quad j = 1, 2, \end{aligned}$$

which play a central role in the design of entropy-conserving and entropy-stable numerical schemes.

For the ideal-gas Euler equations, the physical specific entropy is $s = \log(p \rho^{-\gamma})$. While the Euler system admits a family of entropy pairs [39], the physically relevant entropy for the Navier–Stokes equations with viscosity and heat conduction is uniquely given by [41]

$$(11) \quad \eta = -\frac{\rho s}{\gamma - 1}, \quad \mathbf{q} = -\frac{\rho s \mathbf{u}}{\gamma - 1}.$$

The corresponding entropy variables and potential fluxes are

$$(12) \quad \mathbf{V} = \begin{pmatrix} \frac{\gamma - s}{\gamma - 1} - \frac{|\mathbf{u}|^2}{2c^2} \\ u/c^2 \\ v/c^2 \\ -1/c^2 \end{pmatrix}, \quad \psi = (\psi^f, \psi^g) = \rho \mathbf{u},$$

where $c = \sqrt{\gamma p/\rho}$ denotes the speed of sound. Throughout this paper, we adopt the entropy function (11).

The entropy variables provide a symmetrizing change of variables under which the Euler equations can be written in symmetric form. This structure underpins the continuous entropy analysis and serves as the foundation for the construction of entropy-conserving numerical fluxes and entropy-stable DG discretizations developed in the subsequent sections.

2.2. Formulation in curvilinear coordinates. To construct high-order discretizations on curvilinear meshes, we transform the Euler equations (5) to a reference coordinate system. The spatial domain $\Omega \subset \mathbb{R}^2$ is decomposed into non-overlapping curved quadrilateral elements $\{\Omega_e\}$, each of which is mapped to the reference element $\Omega_{\text{ref}} = [-1, 1]^2$.

Let $(\xi, \eta) \in \Omega_{\text{ref}}$ denote the reference coordinates and $(x^e, y^e) \in \Omega_e$ the corresponding physical coordinates. The element mapping is given by

$$\vec{x}^e(\xi, \eta) = (x^e(\xi, \eta), y^e(\xi, \eta)),$$

where the superscript $(\cdot)^e$ indicates quantities associated with the element Ω_e . Under this mapping, the conservative variables are pulled back to the reference element via

$$\mathbf{U}^e(\xi, \eta) := \mathbf{U}(x^e(\xi, \eta), y^e(\xi, \eta)).$$

Applying the chain rule to (5), the Euler equations on the reference element take the form

$$(13) \quad \mathcal{J}^e \partial_t U_k^e + \partial_\xi \tilde{f}_k^e + \partial_\eta \tilde{g}_k^e = 0, \quad k = 1, 2, 3, 4,$$

where \mathcal{J}^e denotes the Jacobian of the coordinate transformation and $\tilde{f}_k^e, \tilde{g}_k^e$ are the contravariant flux components.

The Jacobian and contravariant fluxes are defined by

$$(14) \quad \begin{aligned} \mathcal{J}^e &= x_\xi^e y_\eta^e - x_\eta^e y_\xi^e, \\ \tilde{f}_k^e(\mathbf{U}^e) &= y_\eta^e f_k(\mathbf{U}^e) - x_\eta^e g_k(\mathbf{U}^e), \quad k = 1, 2, 3, 4, \\ \tilde{g}_k^e(\mathbf{U}^e) &= -y_\xi^e f_k(\mathbf{U}^e) + x_\xi^e g_k(\mathbf{U}^e), \quad k = 1, 2, 3, 4, \end{aligned}$$

where f_k and g_k denote the Cartesian flux components defined in (4).

Since the Jacobian \mathcal{J}^e is generally non-constant, the transformed system (13) constitutes a variable-coefficient hyperbolic system on the reference element.

A fundamental property of smooth coordinate mappings is the satisfaction of the *metric identities*

$$(15) \quad \partial_\xi x_\eta^e = \partial_\eta x_\xi^e, \quad \partial_\xi y_\eta^e = \partial_\eta y_\xi^e,$$

which follow from the commutation of mixed partial derivatives. At the discrete level, however, these identities are not automatically satisfied and must be preserved through a compatible discretization of the geometric terms.

2.3. DG polynomials on the reference element. On the reference element $\Omega_{\text{ref}} = [-1, 1]^2$, we approximate all scalar- and vector-valued quantities by polynomials of degree at most N in each coordinate direction. To this end, we introduce $N + 1$ Legendre–Gauss–Lobatto (LGL) points $\{\xi_i\}_{i=0}^N$ and $\{\eta_j\}_{j=0}^N$ on the interval $[-1, 1]$ in each coordinate direction. Associated with these nodes are the one-dimensional Lagrange interpolation polynomials

$$(16) \quad \phi_j(\xi) = \prod_{\substack{i=0 \\ i \neq j}}^N \frac{\xi - \xi_i}{\xi_j - \xi_i}, \quad j = 0, \dots, N,$$

which satisfy the nodal interpolation property $\phi_j(\xi_i) = \delta_{ij}$.

Using tensor products of the one-dimensional basis functions, we define the nodal polynomial space

$$(17) \quad \mathbb{Q}_N(\Omega_{\text{ref}}) := \text{span} \left\{ \phi_i(\xi)\phi_j(\eta) : 0 \leq i, j \leq N \right\},$$

that is, the space of polynomials of degree at most N in each coordinate direction.

Any scalar function U on Ω_{ref} can be approximated by $U_N \in \mathbb{Q}_N(\Omega_{\text{ref}})$ as

$$(18) \quad U(\xi, \eta) \approx U_N(\xi, \eta) = \sum_{i=0}^N \sum_{j=0}^N U_{i,j} \phi_i(\xi) \phi_j(\eta),$$

where $\{U_{i,j}\}$ are the nodal degrees of freedom (DOFs). In particular, for a component of the conservative variable U_k on physical element Ω_e , we approximate it via the pull back:

$$(19) \quad U_k(x^e(\xi, \eta), y^e(\xi, \eta)) = U_k^e(\xi, \eta) \approx U_{k,N}^e(\xi, \eta) = \sum_{i=0}^N \sum_{j=0}^N (U_k^e)_{i,j} \phi_i(\xi) \phi_j(\eta), \quad k = 1, 2, 3, 4.$$

Moreover, we also use $\mathbb{Q}_N(\Omega_{\text{ref}})$ to approximate flux functions $\mathbf{F}(\mathbf{U})$ via interpolation:

$$(20) \quad \mathbf{F}(\mathbf{U}(x^e(\xi, \eta), y^e(\xi, \eta))) \approx \mathbf{F}_N(\mathbf{U}_N^e)(\xi, \eta) = \sum_{i=0}^N \sum_{j=0}^N \mathbf{F}(\mathbf{U}_{i,j}^e) \phi_i(\xi) \phi_j(\eta).$$

This collocation-based formulation allows all unknowns and fluxes to be represented solely by their values at the LGL nodes.

To approximate derivatives, we introduce the differentiation matrix

$$(21) \quad D_{i,j} = \phi'_j(\xi_i), \quad i, j = 0, \dots, N,$$

so that nodal derivatives in reference space are given by

$$(22) \quad \begin{aligned} \frac{\partial U}{\partial \xi}(\xi_i, \eta_j) &= \sum_{p=0}^N D_{i,p} U_{p,j}, \\ \frac{\partial U}{\partial \eta}(\xi_i, \eta_j) &= \sum_{p=0}^N D_{j,p} U_{i,p}. \end{aligned}$$

The differentiation matrix satisfies the following standard properties.

Lemma 2.1 (Properties of $D_{i,j}$). • *Summation-by-parts (SBP) property:*

$$(23) \quad w_i D_{i,j} + w_j D_{j,i} = \delta_{N,i} \delta_{N,j} - \delta_{0,i} \delta_{0,j}.$$

• *Summation identity:*

$$(24) \quad \sum_{j=0}^N D_{i,j} = 0.$$

The SBP property is the discrete analogue of integration by parts and is central in proving entropy stability.

Remark 2.1 (Discrete metric identities). *At the continuous level, metric identities (15) hold whenever the mapping is sufficiently smooth. At the discrete level, metric identities are not automatically satisfied and must be enforced through a compatible discretization of the geometric terms. One convenient form is*

$$(25) \quad \begin{aligned} \sum_{p_2=0}^N D_{q_2,p_2}(y_\xi)_{q_1,p_2} &= \sum_{p_1=0}^N D_{q_1,p_1}(y_\eta)_{p_1,q_2}, \quad \forall q_1, q_2, \\ \sum_{p_2=0}^N D_{q_2,p_2}(x_\xi)_{q_1,p_2} &= \sum_{p_1=0}^N D_{q_1,p_1}(x_\eta)_{p_1,q_2}, \quad \forall q_1, q_2, \end{aligned}$$

where $(\cdot)_{i,j}$ denotes nodal DOFs of the corresponding geometric derivatives. If the coordinate mapping $(x(\xi, \eta), y(\xi, \eta))$ belongs to $\mathbb{Q}_N(\Omega_{\text{ref}})$, then the discrete metric identities (25) are satisfied automatically when the geometric terms are evaluated using the same LGL interpolation and differentiation operators; see Kopriva [46] for details.

2.4. LGL collocation-based quadrature on the reference element. Let $\{w_i\}_{i=0}^N$ denotes the LGL quadrature weights on the interval $[-1, 1]$. On the reference element $\Omega_{\text{ref}} = [-1, 1]^2$, tensor-product LGL quadrature yields the following approximation of volume integrals:

$$(26) \quad \int_{\Omega_{\text{ref}}} u v d\xi d\eta \approx (u, v)_{\Omega_{\text{ref}}, w} := \sum_{q_1=0}^N \sum_{q_2=0}^N w_{q_1} w_{q_2} u_{q_1, q_2} v_{q_1, q_2}.$$

Boundary integrals on $\partial\Omega_{\text{ref}}$ are approximated using one-dimensional LGL quadrature applied independently on each face. We define the discrete boundary inner product

$$(27) \quad \langle u, v \rangle_{\partial\Omega_{\text{ref}}, w} := \sum_{\gamma \subset \partial\Omega_{\text{ref}}} \sum_{q=0}^N w_q u|_{\gamma, q} v|_{\gamma, q},$$

where γ denotes one of the four faces of Ω_{ref} , and $u|_{\gamma, q}, v|_{\gamma, q}$ denote the evaluation of u and v at the q th LGL node on face γ .

Equivalently, writing the contributions from the four faces explicitly,

$$(28) \quad \begin{aligned} \langle u, v \rangle_{\partial\Omega_{\text{ref}}, w} = \sum_{q=0}^N w_q & \left(u(-1, \eta_q) v(-1, \eta_q) + u(1, \eta_q) v(1, \eta_q) \right. \\ & \left. + u(\xi_q, -1) v(\xi_q, -1) + u(\xi_q, 1) v(\xi_q, 1) \right). \end{aligned}$$

The discrete inner products $(\cdot, \cdot)_{\Omega_{\text{ref}}, w}$ and $\langle \cdot, \cdot \rangle_{\partial\Omega_{\text{ref}}, w}$ are used throughout to approximate volume and surface integrals on the reference element.

3. ENTROPY STABLE DGSEM ON CURVILINEAR MESHES

In this section we describe the discontinuous Galerkin spectral element method (DGSEM) on curvilinear quadrilateral meshes. We first present the standard strong-form DGSEM discretization with LGL quadrature rules, which will serve as the baseline scheme. Next, this formulation will be modified using entropy conserving volume flux to obtain an entropy-stable DG method.

Throughout this section, the spatial domain Ω is decomposed into conforming non-overlapping curved quadrilateral elements $\Omega_h = \{\Omega_e\}_{e=1}^{N_e}$, each mapped to the reference element $\Omega_{\text{ref}} = [-1, 1]^2$. All discretizations are defined elementwise; coupling between elements is achieved through numerical fluxes at shared interfaces.

3.1. Strong-form DGSEM on curvilinear meshes. We discretize the mapped Euler equations (13) on each reference element $\Omega_{\text{ref}} = [-1, 1]^2$, using the contravariant flux formulation introduced in (14). Throughout this section, quantities superscripted by $(\cdot)^e$ are understood to be local to the physical element Ω_e .

The standard nodal DG weak formulation on each element reads as follows: find $\mathbf{U}_N^e = (U_1^e, U_2^e, U_3^e, U_4^e)^T \in [\mathbb{Q}_N(\Omega_{\text{ref}})]^4$ such that, for $k = 1, 2, 3, 4$,

$$(29) \quad \int_{\Omega_{\text{ref}}} \mathcal{J}^e \partial_t U_k^e \hat{\Phi} d\xi d\eta - \int_{\Omega_{\text{ref}}} \tilde{f}_k^e \partial_\xi \hat{\Phi} d\xi d\eta - \int_{\Omega_{\text{ref}}} \tilde{g}_k^e \partial_\eta \hat{\Phi} d\xi d\eta + \int_{\partial\Omega_{\text{ref}}} (\tilde{f}_k^{e,*}, \tilde{g}_k^{e,*}) \cdot \hat{\mathbf{n}} \hat{\Phi} d\hat{s} = 0,$$

for all test functions $\hat{\Phi}(\xi, \eta) \in \mathbb{Q}_N(\Omega_{\text{ref}})$. Here $\hat{\mathbf{n}}$ denotes the outward unit normal vector on the reference boundary $\partial\Omega_{\text{ref}}$, and $\tilde{f}_k^{e,*}, \tilde{g}_k^{e,*}$ are the contravariant numerical fluxes of the form

$$(30) \quad \tilde{f}_k^{e,*} = y_\eta^e f_k^* - x_\eta^e g_k^*, \quad \tilde{g}_k^{e,*} = -y_\xi^e f_k^* + x_\xi^e g_k^*,$$

with the numerical flux $\mathbf{F}_k^* = (f_k^*, g_k^*)^T$ on the physical element Ω_e , to be specified below. The physical conservative variables $U_k(x^e, y^e)$ are recovered from $U_k^e(\xi, \eta)$ via the pull-back mapping (19).

Applying integration by parts to (29) yields the equivalent strong form

$$(31) \quad \int_{\Omega_{\text{ref}}} \mathcal{J}^e \partial_t U_k^e \hat{\Phi} d\xi d\eta + \int_{\Omega_{\text{ref}}} (\partial_\xi \tilde{f}_k^e + \partial_\eta \tilde{g}_k^e) \hat{\Phi} d\xi d\eta - \int_{\partial\Omega_{\text{ref}}} (\tilde{f}_k^e - \tilde{f}_k^{e,*}, \tilde{g}_k^e - \tilde{g}_k^{e,*}) \cdot \hat{\mathbf{n}} \hat{\Phi} d\hat{s} = 0.$$

Next, we approximate the flux functions by polynomial interpolants

$$(32) \quad \tilde{f}_k^e \approx \tilde{f}_{k,N}^e = \sum_{i=0}^N \sum_{j=0}^N (\tilde{f}_k^e)_{i,j} \phi_i(\xi) \phi_j(\eta), \quad \tilde{g}_k^e \approx \tilde{g}_{k,N}^e = \sum_{i=0}^N \sum_{j=0}^N (\tilde{g}_k^e)_{i,j} \phi_i(\xi) \phi_j(\eta),$$

where the nodal contravariant flux values are computed via (14). For example,

$$(\tilde{f}_k^e)_{i,j} = (y_\eta^e)_{i,j} f_k((\mathbf{U}_N^e)_{i,j}) - (x_\eta^e)_{i,j} g_k((\mathbf{U}_N^e)_{i,j}).$$

Next, evaluating the integrals in (31) using the tensor-product LGL quadrature rules (26) and (27) yields the semidiscrete DGSEM scheme

$$(33) \quad \left(\mathcal{J}^e \partial_t U_k^e, \hat{\Phi} \right)_{\Omega_{\text{ref}}, w} + \left((\partial_\xi \tilde{f}_{k,N}^e + \partial_\eta \tilde{g}_{k,N}^e), \hat{\Phi} \right)_{\Omega_{\text{ref}}, w} - \left\langle (\tilde{f}_{k,N}^e - \tilde{f}_k^{e,*}, \tilde{g}_{k,N}^e - \tilde{g}_k^{e,*}) \cdot \hat{\mathbf{n}}, \hat{\Phi} \right\rangle_{\partial\Omega_{\text{ref}}, w} = 0.$$

To motivate the definition of the numerical flux \mathbf{F}_k^* , it is convenient to push forward the reference boundary integral $\left\langle (\tilde{f}_k^{e,*}, \tilde{g}_k^{e,*}) \cdot \hat{\mathbf{n}}, \hat{\Phi} \right\rangle_{\partial\Omega_{\text{ref}}, w}$ to the physical element boundary $\partial\Omega_e$. By definition (30), we obtain

$$(34) \quad \left\langle (\tilde{f}_k^{e,*}, \tilde{g}_k^{e,*}) \cdot \hat{\mathbf{n}}, \hat{\Phi} \right\rangle_{\partial\Omega_{\text{ref}}} = \int_{\partial\Omega_{\text{ref}}} \mathbf{F}_k^* \cdot (\mathcal{J}^e(\mathcal{G}^e)^{-T} \hat{\mathbf{n}}) \hat{\Phi} d\hat{s} = \int_{\partial\Omega_e} \mathbf{F}_k^* \cdot \mathbf{n} \Phi ds,$$

which is the corresponding physical-edge integral. Here $\hat{\Phi}(\xi, \eta) = \Phi(x(\xi, \eta), y(\xi, \eta))$ denotes the standard pull-back of the physical test function to the reference element, and

$$\mathcal{G}^e := \begin{pmatrix} \partial_\xi x & \partial_\xi y \\ \partial_\eta x & \partial_\eta y \end{pmatrix}$$

is the Jacobian matrix of the mapping from reference element Ω_{ref} to physical element Ω_e . The vector $\mathcal{J}^e(\mathcal{G}^e)^{-T} \hat{\mathbf{n}}$ represents the scaled outward normal on the physical edge and satisfies the normal-measure identity

$$(\mathcal{J}^e(\mathcal{G}^e)^{-T} \hat{\mathbf{n}}) d\hat{s} = \mathbf{n} ds.$$

Using the discrete boundary inner product defined in (27), the numerical flux term is approximated by

$$(35) \quad \left\langle (\tilde{f}_k^{e,*}, \tilde{g}_k^{e,*}) \cdot \hat{\mathbf{n}}, \hat{\Phi} \right\rangle_{\partial\Omega_{\text{ref}}} = \sum_{\gamma \subset \partial\Omega_{\text{ref}}} \sum_{q=0}^N w_q \left. \left(\mathbf{F}_k^* \cdot (\mathcal{J}^e(\mathcal{G}^e)^{-T} \hat{\mathbf{n}}) \hat{\Phi} \right) \right|_{\gamma, q},$$

which approximates the physical boundary integral $\int_{\partial\Omega_e} \mathbf{F}_k^* \cdot \mathbf{n} \Phi ds$.

Hence, to evaluate the integral (35), it remains to define the numerical flux in the normal direction on each physical edge. Let $E = \partial\Omega_L \cap \partial\Omega_R$ be an interior edge shared by two elements Ω_L and Ω_R . Denote by \mathbf{U}_L and \mathbf{U}_R the traces of the conservative state on the two sides of E , and let $\mathbf{n} = (n_x, n_y)$ be the unit normal vector on E , oriented from Ω_L to Ω_R . The normal numerical flux is chosen as the local Lax–Friedrichs (Rusanov) flux, defined componentwise by

$$(36) \quad \mathbf{F}_k^* \cdot \mathbf{n} = \frac{1}{2} \left(\mathbf{n} \cdot \mathbf{F}_k(\mathbf{U}_L) + \mathbf{n} \cdot \mathbf{F}_k(\mathbf{U}_R) \right) - \frac{\alpha}{2} \left((U_k)_R - (U_k)_L \right),$$

where the dissipation parameter α is taken as

$$(37) \quad \alpha = \max \{ |\mathbf{u}_L \cdot \mathbf{n}| + c_L, |\mathbf{u}_R \cdot \mathbf{n}| + c_R \},$$

where $\mathbf{u}_{L/R}$ and $c_{L/R}$ denote the velocity vector and sound speed evaluated at the left and right states, respectively.

Choosing the test function in (33) as $\hat{\Phi} = \phi_{p_1}(\xi)\phi_{p_2}(\eta)$ and evaluating the resulting terms yields the nodal (collocation) form of the scheme:

$$(38) \quad \begin{aligned} & w_{p_1} w_{p_2} \mathcal{J}_{p_1, p_2}^e (\partial_t U_k^e)_{p_1, p_2} + w_{p_1} w_{p_2} \sum_{i=0}^N D_{p_1, i} (\tilde{f}_k^e)_{i, p_2} + w_{p_1} w_{p_2} \sum_{j=0}^N D_{p_2, j} (\tilde{g}_k^e)_{p_1, j} \\ & + w_{p_1} \left((\Delta \tilde{g}_k^e)_{p_1, 0} \delta_{p_2, 0} - (\Delta \tilde{g}_k^e)_{p_1, N} \delta_{p_2, N} \right) + w_{p_2} \left((\Delta \tilde{f}_k^e)_{0, p_2} \delta_{p_1, 0} - (\Delta \tilde{f}_k^e)_{N, p_2} \delta_{p_1, N} \right) = 0, \end{aligned}$$

for all $0 \leq p_1, p_2 \leq N$ and $k = 1, 2, 3, 4$, where $\Delta \tilde{f}_k^e = \tilde{f}_k^e - \tilde{f}_k^{e,*}$ and $\Delta \tilde{g}_k^e = \tilde{g}_k^e - \tilde{g}_k^{e,*}$.

The strong-form DGSEM on curvilinear meshes is defined by the semidiscrete scheme (33) together with the local Lax–Friedrichs numerical flux (36). This formulation serves as the baseline DGSEM and provides the foundation for the entropy-stable modifications introduced in the following subsection.

3.2. Entropy stable DGSEM. The strong-form DGSEM discretization introduced in the previous subsection is conservative and high-order accurate, but it does not satisfy a discrete entropy conservation or entropy stability property. In particular, the pointwise evaluation of nonlinear fluxes in the volume terms of (33) prevents the scheme from mimicking the continuous entropy balance, even when entropy-stable numerical fluxes are used at element interfaces.

To obtain an entropy-stable formulation, we follow the entropy framework of Tadmor [68, 69] and exploit the flexibility of nodal DG methods to modify the *volume discretization*. The key idea is to replace the pointwise fluxes in the volume integrals of (33) by symmetric two-point numerical fluxes that are entropy conservative at the discrete level; see, e.g. [8, 9].

We first recall the definition of an entropy-conservative two-point flux.

Definition 3.1. *A two-point numerical volume flux*

$$\mathbf{F}^\#(\mathbf{U}_L, \mathbf{U}_R) = (\mathbf{f}^\#(\mathbf{U}_L, \mathbf{U}_R), \mathbf{g}^\#(\mathbf{U}_L, \mathbf{U}_R))$$

is said to be entropy conservative for the physical flux $\mathbf{F}(\mathbf{U}) = (\mathbf{f}(\mathbf{U}), \mathbf{g}(\mathbf{U}))$ if it satisfies:

- **Consistency:** $\mathbf{F}^\#(\mathbf{U}, \mathbf{U}) = \mathbf{F}(\mathbf{U})$;
- **Symmetry:** $\mathbf{F}^\#(\mathbf{U}_L, \mathbf{U}_R) = \mathbf{F}^\#(\mathbf{U}_R, \mathbf{U}_L)$;
- **Entropy conservation:**

$$(39) \quad (\mathbf{V}_R - \mathbf{V}_L) \cdot \mathbf{F}^\#(\mathbf{U}_L, \mathbf{U}_R) = \boldsymbol{\psi}_R - \boldsymbol{\psi}_L,$$

where \mathbf{V} and $\boldsymbol{\psi} = (\psi^f, \psi^g)$ denote the entropy variables and entropy potential fluxes (12) associated with the entropy function (11).

For the Euler equations, several entropy-conservative two-point fluxes have been proposed in the literature, including the fluxes of Ismail and Roe [42] and Chandrashekar [13]. In this work, we adopt the entropy-conservative flux introduced by Chandrashekar [13], which is also kinetic-energy preserving. Its components are given by

$$(40) \quad \begin{aligned} f_1^\# &= \rho^{\log} \{\{u\}\}, & g_1^\# &= \rho^{\log} \{\{v\}\}, \\ f_2^\# &= \rho^{\log} \{\{u\}\}^2 + \hat{p}, & g_2^\# &= \rho^{\log} \{\{u\}\} \{\{v\}\}, \\ f_3^\# &= \rho^{\log} \{\{u\}\} \{\{v\}\}, & g_3^\# &= \rho^{\log} \{\{v\}\}^2 + \hat{p}, \\ f_4^\# &= \rho^{\log} \{\{u\}\} \hat{h}, & g_4^\# &= \rho^{\log} \{\{v\}\} \hat{h}, \end{aligned}$$

where $f_k^\#$ and $g_k^\#$ denote the components of the numerical fluxes $\mathbf{f}^\#$ and $\mathbf{g}^\#$, respectively.

The arithmetic and logarithmic averages appearing above are defined by

$$(41) \quad \{\{u\}\} = \frac{u_L + u_R}{2}, \quad u^{\log} = \frac{u_L - u_R}{\log(u_L) - \log(u_R)},$$

and the averaged pressure and enthalpy are given by

$$(42) \quad \hat{p} = \frac{\{\{\rho\}\}}{2\{\{\beta\}\}}, \quad \hat{h} = \frac{1}{2\beta^{\log}(\gamma - 1)} - \frac{1}{2}(\{\{u\}\}^2 + \{\{v\}\}^2) + \frac{\hat{p}}{\rho^{\log}} + \{\{u\}\}^2 + \{\{v\}\}^2,$$

where $\beta = \frac{\rho}{2p}$.

Since the entropy-conservative volume fluxes are defined in a two-point fashion, the geometric terms in the contravariant fluxes must be discretized consistently. Following [73], all metric coefficients are replaced by symmetric arithmetic averages, e.g.,

$$(43) \quad \{\{x_\xi\}\}_{L,R} = \frac{1}{2}((x_\xi)_L + (x_\xi)_R).$$

Using these averaged metric terms, the entropy-conservative contravariant volume fluxes are defined as

$$(44) \quad (\tilde{f}_k^{e,\#})_{(i,p_1),p_2} = \{\{y_\eta^e\}\}_{(i,p_1),p_2} (f_k^\#)_{(i,p_1),p_2} - \{\{x_\eta^e\}\}_{(i,p_1),p_2} (g_k^\#)_{(i,p_1),p_2},$$

$$(45) \quad (\tilde{g}_k^{e,\#})_{p_1,(j,p_2)} = -\{\{y_\xi^e\}\}_{p_1,(j,p_2)} (f_k^\#)_{p_1,(j,p_2)} + \{\{x_\xi^e\}\}_{p_1,(j,p_2)} (g_k^\#)_{p_1,(j,p_2)}.$$

The entropy-stable DGSEM is obtained by replacing the volume fluxes in (33) with the entropy-conservative fluxes (44). Specifically, for each element Ω_e , we seek an approximataate solution

$$\mathbf{U}_N^e = (U_1^e, U_2^e, U_3^e, U_4^e)^T \in [\mathbb{Q}_N(\Omega_{\text{ref}})]^4$$

such that for all $0 \leq p_1, p_2 \leq N$ and $k = 1, \dots, 4$, the following semi-discrete formulation holds:

$$(46) \quad \begin{aligned} & w_{p_1} w_{p_2} \left(\mathcal{J}_{p_1,p_2}^e (\partial_t U_k^e)_{p_1,p_2} + 2 \sum_{i=0}^N D_{p_1,i} (\tilde{f}_k^{e,\#})_{(i,p_1),p_2} + 2 \sum_{j=0}^N D_{p_2,j} (\tilde{g}_k^{e,\#})_{p_1,(j,p_2)} \right) \\ & + w_{p_1} ((\Delta \tilde{g}_k^e)_{p_1,0} \delta_{p_2,0} - (\Delta \tilde{g}_k^e)_{p_1,N} \delta_{p_2,N}) + w_{p_2} ((\Delta \tilde{f}_k^e)_{0,p_2} \delta_{p_1,0} - (\Delta \tilde{f}_k^e)_{N,p_2} \delta_{p_1,N}) = 0. \end{aligned}$$

The factor of 2 arises from the symmetric split-form discretization and, together with the SBP property of the differentiation matrices, ensures that the discrete entropy balance mirrors the continuous entropy identity.

The fundamental properties of the resulting entropy-stable DGSEM are summarized below.

Lemma 3.1 (Single-element analysis). *Let $\{\mathbf{U}_N^e\}_e$ denote the numerical solution of the entropy-stable DGSEM (46). On a single element Ω_e , the discrete evolution of the conserved variables satisfies the following relations: for $k = 1, 2, 3, 4$,*

$$(47) \quad \begin{aligned} \sum_{p_1,p_2=0}^N w_{p_1} w_{p_2} \mathcal{J}_{p_1,p_2}^e (\partial_t U_k^e)_{p_1,p_2} &= \sum_{p_1=0}^N w_{p_1} ((\tilde{g}_k^{e,*})_{p_1,0} - (\tilde{g}_k^{e,*})_{p_1,N}) \\ &+ \sum_{p_2=0}^N w_{p_2} ((\tilde{f}_k^{e,*})_{0,p_2} - (\tilde{f}_k^{e,*})_{N,p_2}). \end{aligned}$$

Moreover, the discrete entropy evolves according to

$$(48) \quad \begin{aligned} \sum_{p_1,p_2=0}^N w_{p_1} w_{p_2} \mathcal{J}_{p_1,p_2}^e (\partial_t \eta(\mathbf{U}_N^e))_{p_1,p_2} &= \sum_{p_1=0}^N \sum_{k=1}^4 w_{p_1} ((\tilde{g}_k^{e,*})_{p_1,0} (V_k^e)_{p_1,0} - \tilde{\psi}_{p_1,0}^{e,g}) \\ &- \sum_{p_1=0}^N \sum_{k=1}^4 w_{p_1} ((\tilde{g}_k^{e,*})_{p_1,N} (V_k^e)_{p_1,N} - \tilde{\psi}_{p_1,N}^{e,g}) \\ &+ \sum_{p_2=0}^N \sum_{k=1}^4 w_{p_2} ((\tilde{f}_k^{e,*})_{0,p_2} (V_k^e)_{0,p_2} - \tilde{\psi}_{0,p_2}^{e,f}) \\ &- \sum_{p_2=0}^N \sum_{k=1}^4 w_{p_2} ((\tilde{f}_k^{e,*})_{N,p_2} (V_k^e)_{N,p_2} - \tilde{\psi}_{N,p_2}^{e,f}). \end{aligned}$$

Here, the entropy variables are defined by

$$(V_k^e)_{p_1,p_2} = \left(\frac{\partial \eta}{\partial U_k} (\mathbf{U}_N^e) \right)_{p_1,p_2}, \quad k = 1, \dots, 4,$$

and the contravariant mapped entropy potentials are given by

$$\tilde{\psi}_{p_1, p_2}^{e, f} := (y_\eta^e)_{p_1, p_2} \psi_{p_1, p_2}^f - (x_\eta^e)_{p_1, p_2} \psi_{p_1, p_2}^g, \quad \tilde{\psi}_{p_1, p_2}^{e, g} := -(y_\xi^e)_{p_1, p_2} \psi_{p_1, p_2}^f + (x_\xi^e)_{p_1, p_2} \psi_{p_1, p_2}^g.$$

Proof. The proof closely follows the arguments presented in [26, 25, 73, 28]. For completeness, the proof adapted to the present notation is provided in the Appendix(??). \square

Theorem 3.2 (Multi-element entropy analysis). *Consider the Euler system (5) equipped with periodic boundary conditions, and let $\{\mathbf{U}_N^e\}_e$ denote the solution of the entropy-stable DGSEM (46). Assume that the numerical interface flux (36) is entropy stable in the sense that*

$$(49) \quad (\mathbf{V}_R - \mathbf{V}_L) \cdot (\mathbf{F}^*(\mathbf{U}_L, \mathbf{U}_R) \cdot \mathbf{n}) - (\psi_R - \psi_L) \cdot \mathbf{n} \leq 0,$$

where the unit normal vector \mathbf{n} points from the left state to the right state. Then the DGSEM is entropy stable on the whole computational domain, i.e.,

$$(50) \quad \sum_{e=1}^{N_e} \sum_{p_1, p_2=0}^N w_{p_1} w_{p_2} \mathcal{J}_{p_1, p_2}^e (\partial_t \eta(\mathbf{U}_N^e))_{p_1, p_2} \leq 0.$$

Proof. Using the mapping relation (34), the single-element entropy balance (48) can be expressed in the physical domain as

$$(\eta(\mathbf{U}^e), 1)_{\Omega_e, h} = - \left\langle \sum_{k=1}^4 (\mathbf{F}_k^* \cdot \mathbf{n}) V_k - \psi \cdot \mathbf{n}, 1 \right\rangle_{\partial \Omega_e, h},$$

where $(\cdot, \cdot)_{\Omega_e, h}$ denotes the mapped LGL quadrature on the physical element Ω_e , and $\langle \cdot, \cdot \rangle_{\partial \Omega_e, h}$ denotes the corresponding mapped LGL quadrature on the element boundary $\partial \Omega_e$.

Summing over all elements $\{\Omega_e\}_{e=1}^{N_e}$ and invoking periodic boundary conditions yields

$$\sum_{e=1}^{N_e} (\eta(\mathbf{U}^e), 1)_{\Omega_e, h} = \sum_{E \in \mathcal{E}_h^o} \langle (\mathbf{V}_R - \mathbf{V}_L) \cdot (\mathbf{F}^*(\mathbf{U}_L, \mathbf{U}_R) \cdot \mathbf{n}) - (\psi_R - \psi_L) \cdot \mathbf{n}, 1 \rangle_{E, h},$$

where \mathcal{E}_h^o denotes the set of interior interfaces of the mesh Ω_h . Here, $\mathbf{U}_{L/R}$, $\mathbf{V}_{L/R}$, and $\psi_{L/R}$ denote the left and right traces of the conservative variables, entropy variables, and entropy potentials, respectively, on an interface E .

By the entropy stability assumption (49) on the numerical flux, each interface contribution on the right-hand side is non-positive. Consequently, the global discrete entropy inequality (50) holds, which completes the proof. \square

Remark 3.1 (Entropy stability of Lax–Friedrichs flux). *The local Lax–Friedrichs flux (36) is entropy stable provided that the dissipation parameter α is no smaller than the maximum wave speed of the exact Riemann problem at the interface; see [14] for a detailed discussion. Since computing the exact wave speed is nontrivial [38], we instead adopt the practical wave-speed estimate given in (37). While this choice cannot be theoretically proven to be entropy stable in the sense of (49), it has been observed to behave in an entropy-stable manner in practice.*

We write the semidiscrete entropy-stable DGSEM formulation (46) in the abstract form

$$(51) \quad \frac{d\mathbf{U}_h}{dt} = \mathbf{L}_h(\mathbf{U}_h),$$

where the solution $\mathbf{U}_h \in [V_h]^4$, and V_h is the global discontinuous finite element space defined by

$$V_h := \{v \in L^2(\Omega) : v|_{\Omega^e} \circ \Phi^e \in \mathbb{Q}_N(\Omega_{\text{ref}}), \quad \forall \Omega^e \in \Omega_h\}.$$

Here, $\Phi^e : \Omega_{\text{ref}} \rightarrow \Omega^e$ denotes the element mapping. The operator $\mathbf{L}_h(\cdot)$ represents the spatial discretization defined by the entropy-stable DGSEM formulation.

To advance the semidiscrete system (51) in time, we employ the third-order strong stability preserving Runge–Kutta (SSP-RK3) method [35]. Given the numerical solution \mathbf{U}_h^n at time

level t^n , the solution at the next time level $t^{n+1} = t^n + \Delta t$ is obtained through the following stages:

$$(52) \quad \begin{aligned} \mathbf{U}_h^{(1)} &= \mathbf{U}_h^n + \Delta t \mathbf{L}_h(\mathbf{U}_h^n), \\ \mathbf{U}_h^{(2)} &= \frac{3}{4} \mathbf{U}_h^n + \frac{1}{4} \mathbf{U}_h^{(1)} + \frac{\Delta t}{4} \mathbf{L}_h(\mathbf{U}_h^{(1)}), \\ \mathbf{U}_h^{(3)} &= \frac{1}{3} \mathbf{U}_h^n + \frac{2}{3} \mathbf{U}_h^{(2)} + \frac{2\Delta t}{3} \mathbf{L}_h(\mathbf{U}_h^{(2)}), \\ \mathbf{U}_h^{n+1} &= \mathbf{U}_h^{(3)}. \end{aligned}$$

Remark 3.2 (Positivity preservation). *Due to the use of the Lax–Friedrichs numerical flux (36) in the scheme (46), it can be shown that each stage of the above Runge–Kutta method preserves the positivity of the cell averages of density and pressure under a standard CFL-type time step restriction, following the work of Zhang and Shu [78]; see also [14]. Consequently, a positivity-preserving scaling limiter [78] can be applied to enforce the positivity of density and pressure at all nodal degrees of freedom.*

4. OSCILLATION-ELIMINATING DG (OEDG)

As discussed in the introduction, high-order discontinuous Galerkin approximations may exhibit spurious oscillations in the vicinity of discontinuities. To mitigate these nonphysical oscillations while preserving high-order accuracy in smooth regions, we use the oscillation-eliminating (OE) procedure applied in a post-processing fashion [59].

Let

$$\mathbb{Q}_N(\Omega_e) := \{v \in L^2(\Omega_e) : v \circ \Phi^e \in \mathbb{Q}_N(\Omega_{ref})\}$$

denote the mapped tensor-product polynomial space of degree N on the physical element Ω_e . We define an element-wise linear operator

$$\mathcal{F}_\tau^e : \mathbb{Q}_N(\Omega_e) \longrightarrow \mathbb{Q}_N(\Omega_e),$$

which acts on each component of the DG solution independently. For a solution vector \mathbf{U}_h^e restricted to an element Ω_e , we denote by $U_\sigma^{e,k}(\hat{t}) = \mathcal{F}_\tau^e(U_h^{e,k})$ the OE-processed solution associated with the k -th component, $k = 1, \dots, 4$, where \hat{t} is a pseudo time.

The operator \mathcal{F}_τ^e is defined as the solution of the following initial value problem: for any element Ω_e and each component $k = 1, \dots, 4$,

$$(53) \quad \begin{cases} \frac{d}{d\hat{t}} \int_{\Omega_e} U_\sigma^{e,k} v \, d\mathbf{x} + \sum_{m=0}^N \delta_m^{(e)}(\mathbf{U}_h^e) \int_{\Omega_e} (U_\sigma^{e,k} - P^{m-1} U_\sigma^{e,k}) v \, d\mathbf{x} = 0, & \forall v \in \mathbb{Q}_N(\Omega_e), \\ U_\sigma^{e,k}(\hat{t} = 0) = U_h^{e,k}. \end{cases}$$

Here $\{\delta_m^{(e)}(\mathbf{U}_h^e)\}_{m=0}^N$ are nonnegative strength factors that control the amount of modal damping at different polynomial levels; their precise definition will be given later. $P^m w \in \mathbb{Q}_m(\Omega_e)$ denotes the L^2 projection onto the polynomial space $\mathbb{Q}_m(\Omega_e)$ for $0 \leq m \leq N-1$, defined by

$$(54) \quad \int_{\Omega_e} (P^m w - w) v \, d\mathbf{x} = 0, \quad \forall v \in \mathbb{Q}_m(\Omega_e),$$

and we set $P^{-1} := P^0$ for notational convenience.

The evolution problem (53) is linear and can be solved exactly, making the OE procedure computationally efficient. The specific implementation of the OE operator differs between Cartesian meshes and general curvilinear meshes due to the presence of metric terms. These two cases will be discussed separately in the following subsections.

4.1. OEDG on Cartesian Grids. We first consider the implementation of the OE procedure on Cartesian meshes, where orthogonal modal bases can be exploited to obtain a closed-form expression of the operator $\mathcal{F}_{\hat{t}}$. The presentation follows the general framework of [59], with several modifications tailored to the Cartesian setting.

Let $\{\psi_i(\xi)\}_{i=0}^N$ denote a set of normalized orthogonal polynomials on $[-1, 1]$, such as normalized Legendre polynomials. A tensor-product orthogonal basis on the reference element $\Omega_{\text{ref}} = [-1, 1]^2$ is then given by

$$\Psi_{i,j}(\xi, \eta) := \psi_i(\xi)\psi_j(\eta), \quad 0 \leq i, j \leq N.$$

Using this modal basis, the OE-processed solution $U_{\sigma}^{e,k}$ defined by (53) can be expanded as

$$(55) \quad U_{\sigma}^{e,k}(\hat{t}, \xi, \eta) = \sum_{i,j=0}^N (\hat{U}_{\sigma}^{e,k})_{i,j}(\hat{t}) \Psi_{i,j}(\xi, \eta),$$

where the expansion is performed on the reference element, and the coordinate mapping $(x^e(\xi), y^e(\eta))$ is omitted for brevity.

Due to the hierarchical structure of orthogonal polynomial spaces, the difference between $U_{\sigma}^{e,k}$ and its L^2 projection onto \mathbb{Q}_{m-1} admits the representation

$$(56) \quad U_{\sigma}^{e,k} - P^{m-1}U_{\sigma}^{e,k} = \sum_{\max(i,j) \geq \max\{m, 1\}} (\hat{U}_{\sigma}^{e,k})_{i,j}(\hat{t}) \Psi_{i,j}, \quad m \geq 1.$$

Substituting (56) into (53) and choosing the test function $v = \Psi_{i,j}$ yields a decoupled system of ordinary differential equations for the modal coefficients:

$$(57) \quad \begin{aligned} \frac{d}{d\hat{t}}(\hat{U}_{\sigma}^{e,k})_{i,j} + \left(\sum_{m=0}^{\max(i,j)} \delta_m^{(e)} \right) (\hat{U}_{\sigma}^{e,k})_{i,j} &= 0, \quad \forall \max(i, j) \geq 1, \\ \frac{d}{d\hat{t}}(\hat{U}_{\sigma}^{e,k})_{0,0} &= 0. \end{aligned}$$

Evaluating the solution at pseudo time $\hat{t} = \Delta t$, the above system can be solved exactly as

$$(58) \quad \begin{aligned} (\hat{U}_{\sigma}^{e,k})_{i,j}(\Delta t) &= \exp\left(-\Delta t \sum_{m=0}^{\max(i,j)} \delta_m^{(e)}\right) (\hat{U}_h^{e,k})_{i,j}, \quad \max(i, j) \geq 1, \\ (\hat{U}_{\sigma}^{e,k})_{0,0}(\Delta t) &= (\hat{U}_h^{e,k})_{0,0}. \end{aligned}$$

Consequently, the OE operator on Cartesian grids admits the explicit representation

$$(59) \quad \mathcal{F}_{\Delta t}(U_h^{e,k}) = (\hat{U}_h^{e,k})_{0,0} \Psi_{0,0} + \sum_{\max(i,j) \geq 1} \exp\left(-\Delta t \sum_{m=0}^{\max(i,j)} \delta_m^{(e)}\right) (\hat{U}_h^{e,k})_{i,j} \Psi_{i,j}.$$

We define the damping coefficients $\delta_m^{(e)}$ by

$$(60) \quad \delta_m^{(e)} = \frac{\beta_e}{h_e} \sum_{f \in \partial\Omega_e} \sigma_m^{(f)}(U_h^e),$$

where β_e is an estimate of the local maximum wave speed on Ω_e , and h_e denotes a characteristic element length scale, chosen as the radius of the inscribed circle.

For the compressible Euler equations, we take $\beta_e = \|\bar{\mathbf{u}}\| + \bar{c}$, where $\bar{\mathbf{u}}$ and \bar{c} are the cell-averaged velocity and speed of sound, respectively. The face-based indicator is defined as

$$(61) \quad \sigma_m^{(f)}(U_h^e) = \max_{1 \leq k \leq d} \sigma_m^{(f)}(U_h^{e,k}), \quad f \in \partial\Omega_e,$$

with

$$(62)$$

$$\sigma_m^{(f)}(U_h^{e,k}) = \begin{cases} 0, \\ \frac{(2m+1)h_e^m}{2(2N-1)m!} \left[\sum_{n \leq m} \frac{\frac{1}{|f|} \int_f |\llbracket \partial_x^n U_h^{e,k} \rrbracket_f| dS}{\|U_h^{e,k} - \bar{U}_h^{e,k}\|_{L^\infty(\Omega_e)}} + \sum_{n \leq m} \frac{\frac{1}{|f|} \int_f |\llbracket \partial_y^n U_h^{e,k} \rrbracket_f| dS}{\|U_h^{e,k} - \bar{U}_h^{e,k}\|_{L^\infty(\Omega_e)}} \right], \end{cases} \text{ otherwise.}$$

Remark 4.1 (OE scale factor s). *In practice, the damping induced by (58) may be overly strong for certain problems. To improve accuracy, we introduce a scaling factor $s \in (0, 1)$ and replace the exponential factor in (58) by*

$$(63) \quad \exp\left(-s \Delta t \sum_{m=0}^{\max(i,j)} \delta_m^{(e)}\right).$$

and we will call it OE scale factor s in the following.

Remark 4.2 (Conservation of OE procedure). *Since the modal coefficient $(\hat{U}_h^{e,k})_{0,0}$ is left unchanged, the OE procedure preserves the cell average of each conserved variable, which is a crucial property for stability and conservation.*

Remark 4.3 (Modifications tailored to the Cartesian setting). *Unlike [59], where directional derivatives in all orientations are employed, the Cartesian grid structure allows us to restrict (62) to derivatives aligned with the coordinate directions.*

4.2. OEDG on Curvilinear Grids.

4.2.1. *Exact solution of (53).* On general curvilinear meshes, constructing a local orthogonal modal basis on each element Ω_e is impractical due to the metric terms. Nevertheless, the projection operators P^m defined in (54) remain well-defined on Ω_e . We approximate the integrals in (54) using the LGL rule of degree N (26). We therefore derive an explicit expression for the OE operator $\mathcal{F}_{\Delta t}^e$ using only the nested structure of polynomial spaces.

Recall the hierarchy

$$\mathbb{Q}_0(\Omega_e) \subset \mathbb{Q}_1(\Omega_e) \subset \cdots \subset \mathbb{Q}_N(\Omega_e).$$

For any $u \in \mathbb{Q}_N(\Omega_e)$, define the incremental (projection-difference) components

$$(64) \quad u_0 := P^0 u, \quad \Delta_k := P^k u - P^{k-1} u, \quad k = 1, \dots, N,$$

so that the telescoping decomposition holds:

$$(65) \quad u = u_0 + \sum_{k=1}^N \Delta_k.$$

Note that $\Delta_k \in \mathbb{Q}_k(\Omega_e)$ and $P^{k-1} \Delta_k = 0$, hence Δ_k lies in the complement $\mathbb{W}_k := \mathbb{Q}_k \ominus \mathbb{Q}_{k-1}$ in the L^2 sense. The following lemmas summary some useful properties of Δ_k .

Lemma 4.1. *For each $k = 1, \dots, N$, the increment Δ_k is L^2 -orthogonal to $\mathbb{Q}_{k-1}(\Omega_e)$, i.e.,*

$$\int_{\Omega_e} \Delta_k v \, d\mathbf{x} = 0, \quad \forall v \in \mathbb{Q}_{k-1}(\Omega_e).$$

Lemma 4.2. *For $k = 1, \dots, N$ and any $m \geq 0$,*

$$(I - P^{m-1}) \Delta_k = \begin{cases} 0, & m-1 \geq k, \\ \Delta_k, & m \leq k, \end{cases} \quad \text{and} \quad (I - P^{m-1}) u_0 = 0.$$

Proof. Since $\Delta_k = P^k u - P^{k-1} u$ and P^{m-1} is a projection, if $m-1 \geq k$ then $P^{m-1} P^k u = P^k u$ and $P^{m-1} P^{k-1} u = P^{k-1} u$, hence $P^{m-1} \Delta_k = \Delta_k$ and $(I - P^{m-1}) \Delta_k = 0$.

If $m \leq k$, then $P^{m-1} P^k u = P^{m-1} u = P^{m-1} P^{k-1} u$, so $P^{m-1} \Delta_k = 0$ and $(I - P^{m-1}) \Delta_k = \Delta_k$.

Finally, $u_0 \in \mathbb{Q}_0$ implies $P^{m-1} u_0 = u_0$ for all m , hence $(I - P^{m-1}) u_0 = 0$. \square

We now derive the explicit solution of the OE evolution (53). Consider a scalar component on Ω_e and write $u_\sigma(\hat{t}) = \mathcal{F}_{\hat{t}}(u)$. Substituting (65) into (53) and using Lemma 4.2 gives, for all $v \in \mathbb{Q}_N(\Omega_e)$,

$$(66) \quad \frac{d}{d\hat{t}} \int_{\Omega_e} \left(u_0 + \sum_{k=1}^N \Delta_k(\hat{t}) \right) v \, d\mathbf{x} + \sum_{k=1}^N \left(\sum_{m=0}^k \delta_m^{(e)}(u) \right) \int_{\Omega_e} \Delta_k(\hat{t}) v \, d\mathbf{x} = 0.$$

The key observation is that (66) decouples across the nested subspaces. Fix $\ell \in \{0, 1, \dots, N\}$ and choose $v \in \mathbb{Q}_\ell(\Omega_e)$. By Lemma 4.1, we have $\int_{\Omega_e} \Delta_k v \, d\mathbf{x} = 0$ for all $k \geq \ell + 1$, hence (66) reduces to

$$(67) \quad \frac{d}{d\hat{t}} \int_{\Omega_e} \left(u_0 + \sum_{k=1}^{\ell} \Delta_k(\hat{t}) \right) v \, d\mathbf{x} + \sum_{k=1}^{\ell} \left(\sum_{m=0}^k \delta_m^{(e)}(u) \right) \int_{\Omega_e} \Delta_k(\hat{t}) v \, d\mathbf{x} = 0, \quad \forall v \in \mathbb{Q}_\ell(\Omega_e).$$

Subtracting the same identity written for $\ell - 1$ from that for ℓ and using the fact that $\mathbb{Q}_{\ell-1} \subset \mathbb{Q}_\ell$ yields an evolution equation on the increment subspace \mathbb{W}_ℓ . Equivalently, (53) induces the following *strong* ODE for each increment Δ_ℓ :

$$(68) \quad \frac{d}{d\hat{t}} \Delta_\ell(\hat{t}) + \left(\sum_{m=0}^{\ell} \delta_m^{(e)}(u) \right) \Delta_\ell(\hat{t}) = 0, \quad \ell = 1, \dots, N,$$

together with $\frac{d}{d\hat{t}} u_0 = 0$. Therefore,

$$(69) \quad u_\sigma(\Delta t) = u_0 + \sum_{k=1}^N \exp \left(-\Delta t \sum_{m=0}^k \delta_m^{(e)}(u) \right) \Delta_k.$$

In particular, the constant component $u_0 = P^0 u$ (hence the cell average) is preserved exactly.

Finally, for the Euler system on Ω_e , the operator is applied component-wise. Denoting $\mathbf{U}_\sigma^e = \mathcal{F}_{\Delta t}(\mathbf{U}_h^e)$, we have for each component $r = 1, \dots, 4$,

$$(70) \quad U_\sigma^{e,r} = P^0(U_h^{e,r}) + \sum_{k=1}^N \exp \left(-\Delta t \sum_{m=0}^k \delta_m^{(e)}(\mathbf{U}_h^e) \right) (P^k(U_h^{e,r}) - P^{k-1}(U_h^{e,r})).$$

4.2.2. Damping coefficients. The damping coefficients $\delta_m^{(e)}$ appearing in (70) are constructed from face-based jump indicators. As in the Cartesian case, we first define for each face $f \subset \partial\Omega_e$,

$$(71) \quad \sigma_m^{(f)}(\mathbf{U}_h^e) = \max_{1 \leq r \leq 4} \sigma_m^{(f)}(U_h^{e,r}), \quad f \in \partial\Omega_e,$$

where $U_h^{e,r}$ denotes the r -th component of the Euler state.

For each scalar component $U_h^{e,r}$, we set

$$(72) \quad \sigma_m^{(f)}(U_h^{e,r}) = \begin{cases} 0, & U_h^{e,r} = \bar{U}_h^{e,r}, \\ \frac{(2m+1) h_e^m}{2(2N-1) m!} \sum_{|\boldsymbol{\alpha}| \leq m} \frac{\frac{1}{|f|} \int_f \left| \llbracket \partial^{\boldsymbol{\alpha}} U_h^{e,r} \rrbracket_f \right| dS}{\|U_h^{e,r} - \bar{U}_h^{e,r}\|_{L^\infty(\Omega_e)}}, & \text{otherwise,} \end{cases}$$

where $\boldsymbol{\alpha} = (\alpha_1, \alpha_2)$ is a multi-index with $|\boldsymbol{\alpha}| = \alpha_1 + \alpha_2$, and

$$\partial^{\boldsymbol{\alpha}} U := \frac{\partial^{|\boldsymbol{\alpha}|} U}{\partial x^{\alpha_1} \partial y^{\alpha_2}}.$$

All remaining quantities (jump operator $\llbracket \cdot \rrbracket_f$, face measure $|f|$, and element length scale h_e) follow the definitions in (62).

4.2.3. *Shock indicator and selective application of OE.* On curvilinear meshes, evaluating (72) can be computationally expensive because it requires mixed derivatives up to order m on every face and for every state component. In our experiments, the OE stage may account for a substantial fraction of the overall runtime. To reduce the cost, we apply OE only on *troubled elements* detected by a shock indicator.

Among many available indicators [47, 29, 61], we adopt a low-cost choice derived from the zero-order jump measure in (72). Specifically, for each element Ω_e we define

$$(73) \quad \mathcal{I}^{(e)}(\mathbf{U}_h^e) = \sum_{f \in \partial\Omega_e} \sigma_0^{(f)}(\mathbf{U}_h^e),$$

with $\sigma_0^{(f)}(\mathbf{U}_h^e)$ given by (71) at $m = 0$, i.e.,

$$(74) \quad \sigma_0^{(f)}(\mathbf{U}_h^{e,r}) = \begin{cases} 0, & \mathbf{U}_h^{e,r} = \bar{\mathbf{U}}_h^{e,r}, \\ \frac{1}{2(2N-1)} \frac{\frac{1}{|f|} \int_f |\llbracket \mathbf{U}_h^{e,r} \rrbracket_f| dS}{\|\mathbf{U}_h^{e,r} - \bar{\mathbf{U}}_h^{e,r}\|_{L^\infty(\Omega_e)}}, & \text{otherwise.} \end{cases}$$

Elements satisfying the following conditions are marked as troubled and subjected to the full OE operator:

$$(75) \quad \mathcal{I}^{(e)}(\mathbf{U}_h^e) > C$$

where constant C is named as shock indicator threshold in the following. Otherwise we set $\mathbf{U}_\sigma^e = \mathbf{U}_h^e$.

Algorithm 1: Selective OE procedure on curvilinear meshes using a shock indicator.

Input : DG solution $\{\mathbf{U}_h^e\}_e$; threshold constant $C > 0$.

Output: OE-processed solution $\{\mathbf{U}_\sigma^e\}_e$.

```

1 foreach element  $\Omega_e$  do
2   | Compute  $\mathcal{I}^{(e)}(\mathbf{U}_h^e)$  from (73)–(74)
3   | if  $\mathcal{I}^{(e)}(\mathbf{U}_h^e) > C$  then
4   |   | Compute  $\sigma_m^{(f)}(\mathbf{U}_h^e)$  for  $m = 1, \dots, N$  via (72)
5   |   | Form  $\delta_m^{(e)}$  and apply (70) to obtain  $\mathbf{U}_\sigma^e$ 
6   | else
7   |   | Set  $\mathbf{U}_\sigma^e \leftarrow \mathbf{U}_h^e$ 
8   | end
9 end

```

Remark 4.4 (Comparision with KXRCF indicator). *The indicator (73) is closely related in structure to jump-based sensors such as the KXRCF indicator [47] and several recent variants [72]. This motivates the use of $\sigma_0^{(f)}$ as a cost-effective troubled-cell detector.*

5. NUMERICAL EXAMPLES

In this section, we use multiple numerical examples to assess the performance of the proposed entropy-stable DG scheme equipped with the oscillation-eliminating (OE) procedure on both Cartesian and curvilinear meshes. Unless otherwise specified, a positivity-preserving limiter [78, 77] is applied in all numerical experiments to guarantee non-negativity of the density and pressure. The code implementation is based on MFEM library [3, 4] for all the simulations.

Time integration is performed using the third-order strong-stability-preserving Runge–Kutta method (52). The time step size Δt is determined according to the CFL condition

$$(76) \quad \Delta t = K \min_{\Omega_e} \frac{h_e}{(\|\mathbf{u}_e\| + c_e)},$$

where K is the CFL constant, h_e denotes a characteristic element length scale (taken as the radius of the inscribed circle of Ω_e), and \mathbf{u}_e and c_e are the local velocity vector and speed of sound on element Ω_e , respectively. In practice, \mathbf{u}_e and c_e are evaluated by taking the maximum

over the quadrature points within each element. In all the following simulations and tests, we use CFL constant $K = \frac{0.5}{2N+1}$. Unless otherwise specified, the OE scale factor s defined in (63) and shock indicator threshold C defined in (75) are set as:

$$(77) \quad s = 0.2, \quad C = 0.02.$$

5.1. Isentropic Euler vortex problem. The isentropic Euler vortex problem describes the advection of a smooth vortex by a constant background velocity field. Owing to its known analytic solution, this problem serves as a standard benchmark for assessing the accuracy and robustness of high-order numerical methods for the compressible Euler equations [71, 67].

The computational domain is the periodic square $\Omega = [-10, 10]^2$. The exact solution is given by

$$(78) \quad \begin{aligned} u(x, y, t) &= u_b - \frac{\beta}{2\pi} (y - v_b t) \exp\left(\frac{1}{2} \left[1 - (x - u_b t)^2 - (y - v_b t)^2\right]\right), \\ v(x, y, t) &= v_b + \frac{\beta}{2\pi} (x - u_b t) \exp\left(\frac{1}{2} \left[1 - (x - u_b t)^2 - (y - v_b t)^2\right]\right), \\ T(x, y, t) &= 1 - \frac{(\gamma - 1)\beta^2}{8\gamma\pi^2} \exp(1 - (x - u_b t)^2 - (y - v_b t)^2), \\ \rho(x, y, t) &= T(x, y, t)^{\frac{1}{\gamma-1}}, \quad p(x, y, t) = T(x, y, t)^{\frac{\gamma}{\gamma-1}}. \end{aligned}$$

Here $\gamma = 1.4$ is the ratio of specific heats, $\beta = 5$ controls the vortex strength, and $(u_b, v_b) = (1, 1)$ denotes the constant background velocity.

To assess the performance of the proposed method on curved geometries, we employ a curvilinear mesh in this test. The mesh is generated by first constructing a uniform Cartesian grid with $N_x = N_y = M$ elements, and then applying the smooth coordinate transformation

$$(79) \quad \begin{aligned} x' &= x + 0.05 \sin(\alpha\pi x) \cos(\alpha\pi y), \\ y' &= y + 0.10 \cos(\alpha\pi x) \sin(\alpha\pi y), \end{aligned}$$

with $\alpha = 1.5$.

Figure 1 illustrates the initial density field together with the resulting curvilinear mesh.

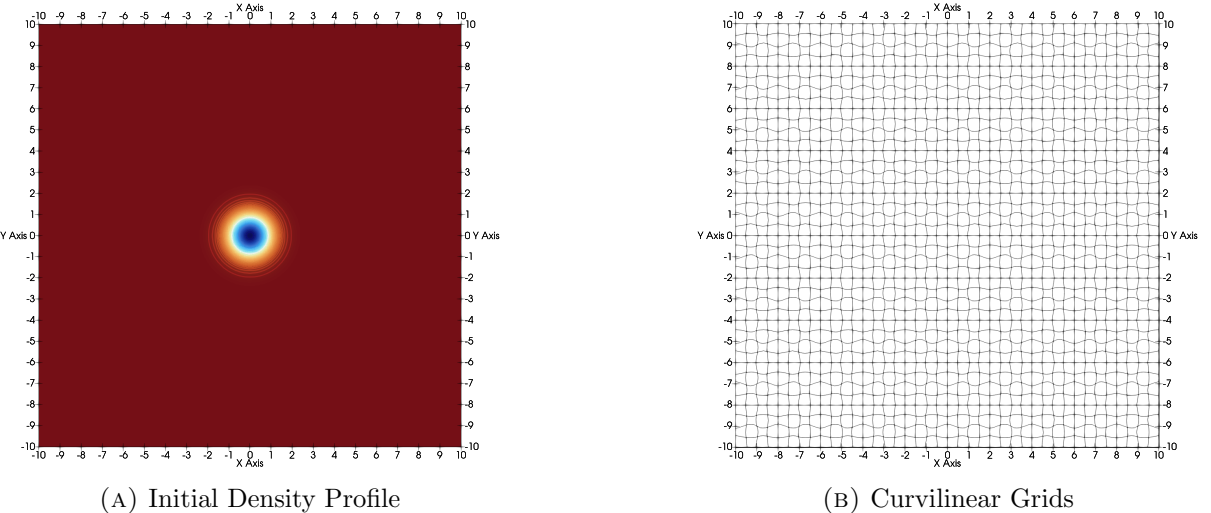


FIGURE 1. *Isentropic Euler vortex problem:* initial condition of density and Curvilinear grids for Isentropic Euler Vortex problem. Mesh size: $N_x = N_y = M = 40$

To assess the convergence behavior, the simulation is advanced to $t = 20$, corresponding to one full advection period of the vortex across the domain. The L^2 errors of all conservative

variables are then computed for polynomial orders $N = 3$ and $N = 4$ in \mathbb{Q}_N . Note that due to smoothness of this test case, the OE procedure is not activated.

Figure 2 demonstrates that the proposed method achieves the expected $(N + 1)$ -th order convergence rate, i.e., $\mathcal{O}(h^{N+1})$, where the mesh size is defined as $h = 20/M$. This behavior is consistent with the theoretical convergence results for smooth solutions of the discontinuous Galerkin method [17].

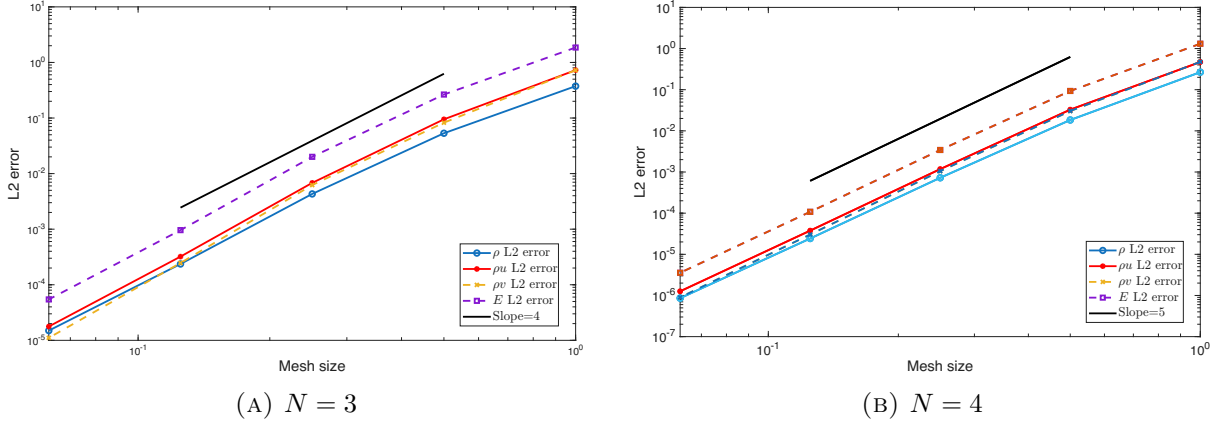


FIGURE 2. *Isentropic Euler vortex problem*: convergency Rate of Isentropic Euler vortex problem in curvilinear mesh. Left figure has polynomial order of $N = 3$, and the polynomial order of right figure is $N = 4$

We further examine the entropy stability of the proposed scheme for this test case. Specifically, we compute the numerical approximation of the total entropy

$$(80) \quad I_\eta(t) = \int_{\Omega} \eta \, d\mathbf{x} = \sum_e \int_{\Omega_e} \eta \, d\mathbf{x},$$

and track its evolution in time.

Figure 3 shows the time history of $I_\eta(t)$. In both cases, the total entropy is observed to be non-increasing throughout the simulation, indicating that the proposed DG scheme satisfies a discrete entropy inequality and is therefore entropy stable.

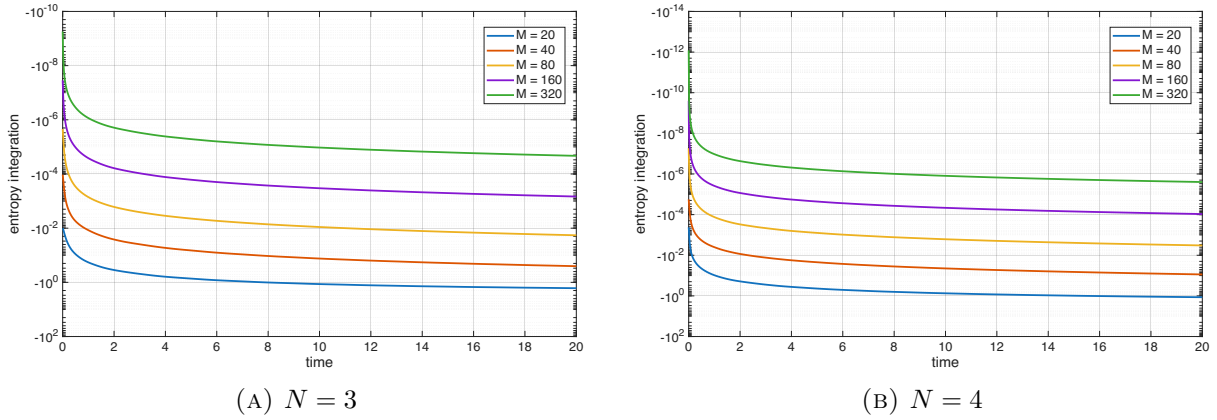


FIGURE 3. *Isentropic Euler vortex problem*: how entropy integration changes with time. Left figure has polynomial order of $N = 3$, and the polynomial order of right figure is $N = 4$

5.2. Two-dimensional Riemann problems. We next consider two-dimensional Riemann problems for the compressible Euler equations. The computational domain $\Omega = [0, 1]^2$ is divided into four quadrants, each of which is assigned a constant initial state. Depending on the choice

of these initial states, a wide variety of wave interactions and flow structures can be generated [49, 65]. In this work, we focus on Riemann problems 12 and 13 reported in [49].

In several existing studies, outflow boundary conditions are employed for these problems [59]. However, in our numerical experiments, such boundary conditions may induce spurious oscillations near the domain boundaries. To avoid these effects and to better isolate the interior wave interactions, we instead impose periodic boundary conditions as described in [37].

To accommodate periodic boundaries, the computational domain is extended to $\Omega = [0, 2]^2$, and the initial data are defined through a periodic extension of the standard Riemann configuration on $[0, 1]^2$. Specifically, the initial condition is given by

$$(81) \quad \begin{aligned} \mathbf{U} &= \mathbf{U}_1, & 0 < x < 0.5, 0 < y < 0.5, \\ \mathbf{U} &= \mathbf{U}_2, & 0 < x < 0.5, 0.5 < y < 1, \\ \mathbf{U} &= \mathbf{U}_3, & 0.5 < x < 1, 0 < y < 0.5, \\ \mathbf{U} &= \mathbf{U}_4, & 0.5 < x < 1, 0.5 < y < 1, \\ \mathbf{U}(x, y) &= \mathbf{U}(x, 2 - y), & 0 < x < 1, 1 < y < 2, \\ \mathbf{U}(x, y) &= \mathbf{U}(2 - x, y), & 1 < x < 2, 0 < y < 1, \\ \mathbf{U}(x, y) &= \mathbf{U}(2 - x, 2 - y), & 1 < x < 2, 1 < y < 2. \end{aligned}$$

Here $\mathbf{U} = (\rho, \rho u, \rho v, E)^\top$ denotes the vector of conservative variables, and $\mathbf{U}_1, \mathbf{U}_2, \mathbf{U}_3, \mathbf{U}_4$ are the prescribed constant states defining the corresponding two-dimensional Riemann problem on the unit square $[0, 1]^2$.

For the following two Riemann problems, computations are performed on uniform Cartesian grids with $N_x = N_y = 320$ elements. In both of the two following two problems, we use the \mathbb{Q}_3 DG approximation on all element.

5.2.1. Two-dimensional Riemann problem: Case 12. We first consider Riemann problem 12 from [49]. The initial conditions on the unit square $[0, 1]^2$ are prescribed as

$$(82) \quad \begin{aligned} \rho &= 0.8, & p &= 1.0, & \mathbf{u} &= (0, 0), & 0 < x < 0.5, 0 < y < 0.5, \\ \rho &= 1.0, & p &= 1.0, & \mathbf{u} &= (0.7276, 0), & 0 < x < 0.5, 0.5 < y < 1, \\ \rho &= 1.0, & p &= 1.0, & \mathbf{u} &= (0, 0.7276), & 0.5 < x < 1, 0 < y < 0.5, \\ \rho &= 0.5313, & p &= 0.4, & \mathbf{u} &= (0, 0), & 0.5 < x < 1, 0.5 < y < 1. \end{aligned}$$

These states define the vectors $\mathbf{U}_1, \mathbf{U}_2, \mathbf{U}_3$, and \mathbf{U}_4 in (81). The initial condition on the extended domain $\Omega = [0, 2]^2$ is then obtained via the periodic extension described in (81).

The simulation is advanced to $t = 0.2$. The numerical results for Riemann problem 12 are shown in Figure 4. The results are clipped to the domain $[0, 1]^2$. In Figure 4(a), the density profiles demonstrate that the contact discontinuity in the lower-left quadrant is well resolved, and the fine-scale flow structures behind the shocks are well captured. These features are in good agreement with previously reported results [49, 65, 48].

Figure 4(b) displays the distribution of the shock indicator defined in (73) and (74). The indicator is activated primarily in regions containing strong shocks, while remaining inactive in smooth regions. As a result, the OE procedure is applied only where necessary, leading to a significant reduction in its computational cost.

5.2.2. Two-dimensional Riemann problem: Case 13. Then Riemann problem 13 from [49] is considered. The initial condition on the unit square $[0, 1]^2$ is set as:

$$(83) \quad \begin{aligned} \rho &= 0.8, & p &= 0.4, & \mathbf{u} &= (0.1, -0.3), & \text{in } 0 < x < 0.5, 0 < y < 0.5, \\ \rho &= 0.5197, & p &= 0.4, & \mathbf{u} &= (-0.6259, -0.3), & \text{in } 0 < x < 0.5, 0.5 < y < 1, \\ \rho &= 0.5313, & p &= 0.4, & \mathbf{u} &= (0.1, 0.4276), & \text{in } 0.5 < x < 1, 0 < y < 0.5, \\ \rho &= 1, & p &= 1, & \mathbf{u} &= (0.1, -0.3), & \text{in } 0.5 < x < 1, 0.5 < y < 1, \end{aligned}$$

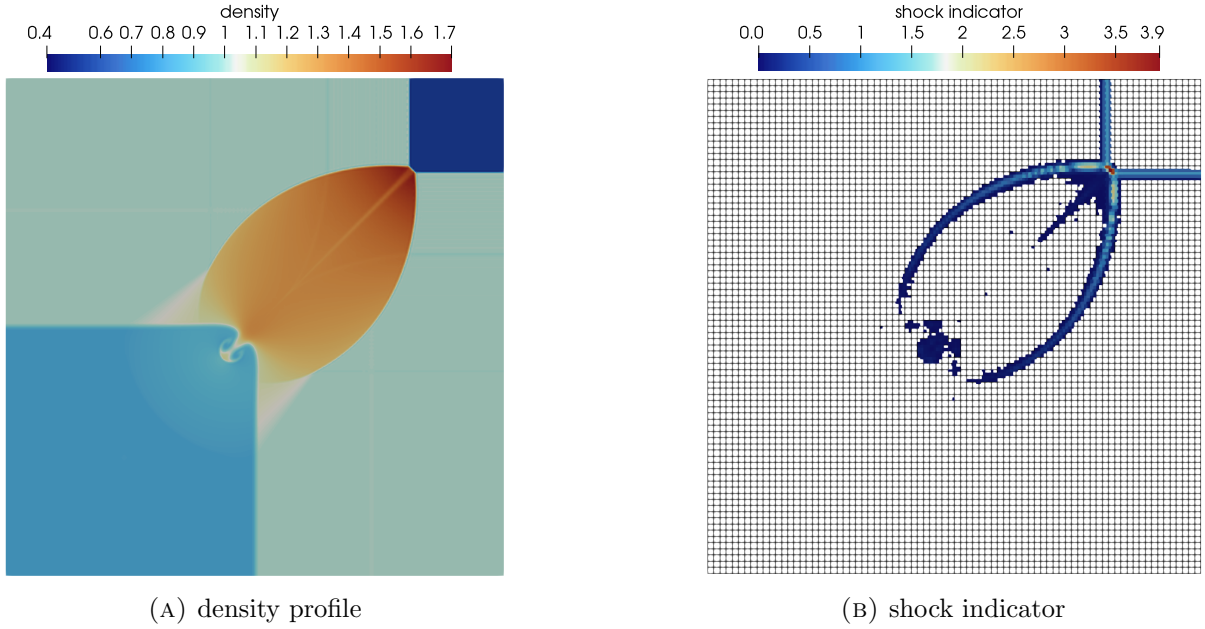


FIGURE 4. *Two-dimensional Riemann problem 12*: (a) the density profile at $t = 0.2$; (b) the shock indicator profile at $t = 0.2$.

For this test, we run the simulation to $t = 0.3$. Figure 5 shows the solution of Riemann problem 13 clipped to the domain $[0, 1]^2$. Figure 5(a) shows the density profile, where the shocks and contact discontinuities are captured well. Figure 5(b) shows the profile of shock indicator.

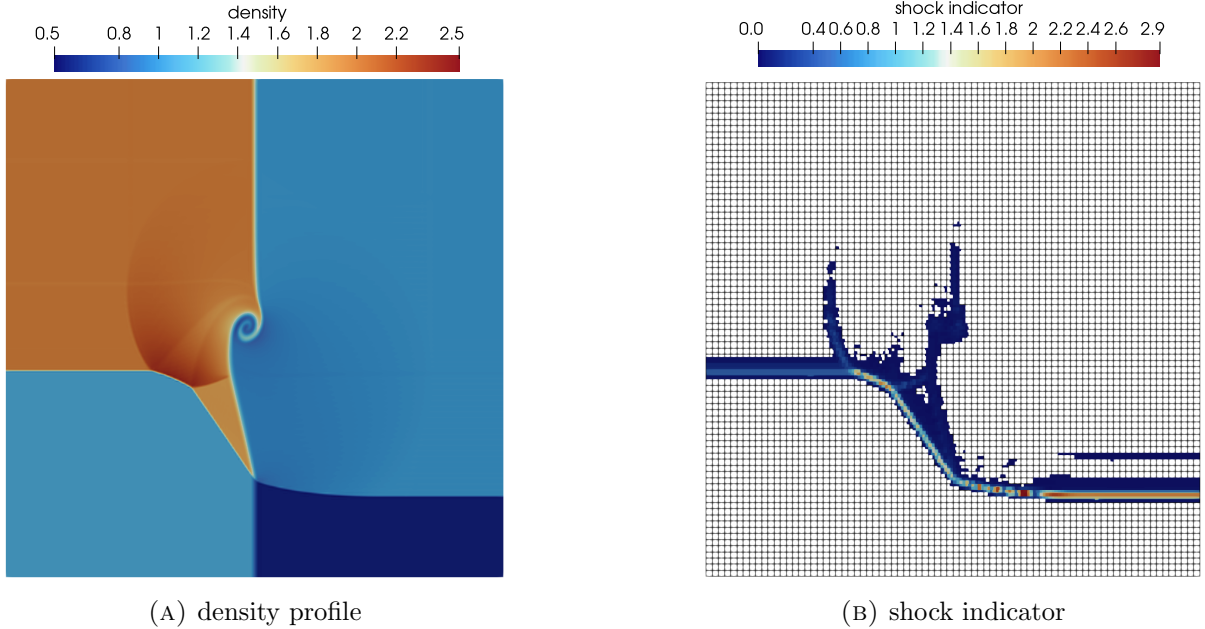


FIGURE 5. *Two-dimensional Riemann problem 13*: (a) the density profile at $t = 0.3$; (b) the shock indicator profile at $t = 0.3$.

5.3. Double Mach Reflection. The double Mach reflection problem is a classical benchmark for evaluating the performance of numerical schemes in the presence of strong shocks and complex wave interactions. Owing to its rich flow features, including shock–shock interactions and shear-layer instabilities, this problem has been extensively studied in the literature [74, 66, 77].

The computational domain is the rectangular region $\Omega = [0, 4] \times [0, 1]$. The initial condition consists of an oblique shock with Mach number 10 propagating to the right. The shock initially

intersects the bottom boundary at $(x, y) = (1/6, 0)$ and forms an angle of 60° with respect to the horizontal direction. The corresponding initial states are given by

$$(84) \quad (\rho, u, v, p) = \begin{cases} (8, 8.25 \cos(\pi/6), -8.25 \sin(\pi/6), 116.5), & x < \frac{1}{6} + \frac{y}{\sqrt{3}}, \\ (1.4, 0, 0, 1), & x > \frac{1}{6} + \frac{y}{\sqrt{3}}. \end{cases}$$

The boundary conditions are prescribed as follows. An inflow condition is imposed on the left boundary, while an outflow condition is used on the right boundary. On the top boundary, a moving shock condition is applied: the post-shock state is prescribed on the segment $0 < x < \frac{1}{6} + \frac{1}{\sqrt{3}}(1 + 20t)$, and the pre-shock state is used elsewhere. On the bottom boundary, the post-shock state is imposed for $0 < x < \frac{1}{6}$, whereas a reflective wall boundary condition is applied on the remaining portion.

The computation is carried out on a uniform Cartesian grid with $N_x = 480$ and $N_y = 120$ elements, corresponding to a mesh size $h_x = h_y = 1/120$. A Q_2 DG approximation is employed on all elements. The OE parameters s and C are set as (77).

Figure 6 presents the numerical results at time $t = 0.2$. Figure 6(a) shows the density contours in the region $[0, 3] \times [0, 1]$, where nonphysical oscillations near strong discontinuities are effectively suppressed by the OE procedure. Figure 6(b) displays a zoomed-in view of the density field over $[2.2, 2.8] \times [0, 0.5]$, revealing fine-scale flow structures, including small roll-ups associated with Kelvin–Helmholtz instabilities. In contrast, such details are significantly damped in [59] due to stronger numerical dissipation.

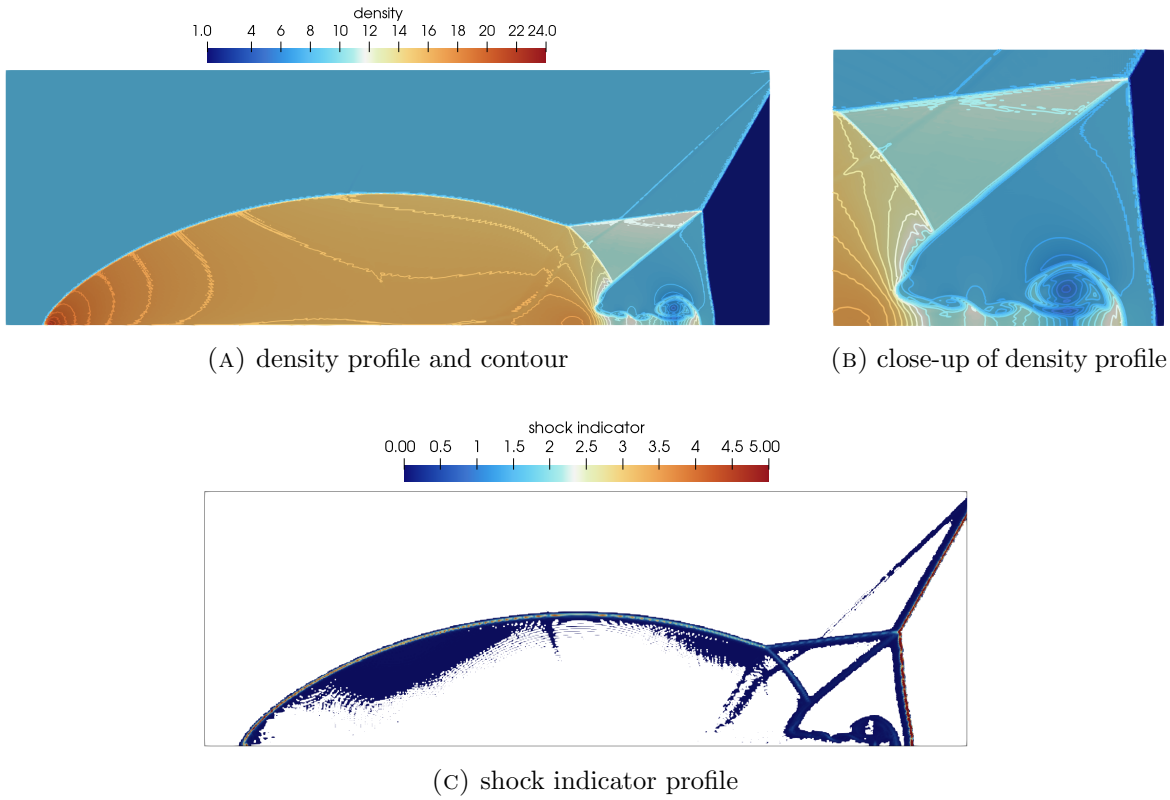


FIGURE 6. *Double Mach Reflection*: (a) the density profile and contour in $[0, 3] \times [0, 1]$ at $t = 0.2$. The contour shown in the image is generated from 35 evenly distributed contours; (b) the close-up of density profile in $[2.2, 2.8] \times [0, 0.5]$ at $t = 0.2$; (c) the shock indicator profile.

We further investigate the influence of the shock-indicator threshold C on the computational cost. All parameters are identical to those used in Figure (6), except that the threshold is

varied as $C = 0, 0.02$, and 0.1 . Table (1) reports the corresponding computational statistics. The average CPU time per time step is defined as $\frac{\text{total CPU time}}{\text{total step}}$.

As shown in Table (1), increasing the threshold C leads to a reduction in computational cost. This behavior is expected, since a larger threshold identifies fewer troubled cells and therefore reduces the number of elements where the OE procedure is activated. These results confirm that the shock-indicator strategy effectively improves the efficiency of the OE procedure.

For comparison, the last row of Table (1) corresponds to a computation performed without the OE procedure. In this case, the average CPU time per step is significantly smaller, due to the absence of additional damping operations. However, the total number of time steps — and consequently the total CPU time — is larger than in the stabilized cases. This is because uncontrolled numerical oscillations enforce smaller admissible time steps, thereby increasing the overall computational effort. Figure (7) presents the density fields and corresponding shock-

	total step	total CPU time	average CPU time per step
$C = 0$	10261	3123.8 s	0.304 s
$C = 0.02$	10261	2570.3 s	0.250 s
$C = 0.1$	10302	2128.3 s	0.206 s
no OE	40622	4029.0 s	0.099 s

TABLE 1. *Double Mach Reflection*: comparison of computation time with different shock indicator threshold C . In the last row, the OE procedure is not used.

indicator distributions for $C = 0, 0.02$, and 0.1 . The density solutions obtained with different threshold values exhibit only minor differences, indicating that moderate variations of C do not significantly affect the resolved flow structures. In contrast, the solution computed without the OE procedure exhibits pronounced nonphysical oscillations, highlighting the necessity of oscillation control for robust simulations.

5.4. Supersonic Flow Around a Two-Dimensional Cylinder. We next consider the problem of supersonic flow past a circular cylinder, which has been extensively studied in the literature [36, 21, 58, 16]. This is a highly challenging benchmark, as it involves multiple interacting flow features, including a strong bow shock, oblique shocks, a downstream “fishtail” shock, Kelvin–Helmholtz instabilities, and their nonlinear interactions. Accurately resolving these phenomena requires a numerical method that is both robust and minimally dissipative.

The computational domain is the rectangular region $\Omega = [-0.6, 3.4] \times [-1, 1]$, containing a circular cylinder of diameter $D = 0.5$ centered at $(0, 0)$. The mesh is generated using the open-source software **Gmsh** [33, 63]. We employ high-order curvilinear quadrilateral elements whose geometric order matches the polynomial degree of the DG approximation space \mathbb{Q}_N . The mesh is generated with a characteristic mesh size of $h = 0.0085$, and consists of 126,082 elements. Using third-order elements ($N = 3$), the total number of degrees of freedom is 2,017,312.

The initial condition corresponds to a uniform Mach 3 supersonic inflow with $\rho = 1$, $p = 1$, and velocity $\mathbf{u} = (3.55, 0)$. Inflow and outflow boundary conditions are imposed on the left and right boundaries, respectively. Slip wall (reflective) boundary conditions are applied on the upper and lower boundaries, as well as on the surface of the cylinder. We use \mathbb{Q}_3 for the DG approximation polynomial. Here, we vary the OE scale factor s to examine its impact on the performance of the OE procedure described in Algorithm 1. The shock indicator threshold remains fixed at $C = 0.02$.

Figure 8 presents results obtained with OE scaling factor $s = 0.1$ at times $t = 0.5, 2.5, 3.0$, and 4.5 , together with the corresponding shock indicator distributions. To highlight the shock structures and shear layers, the flow field is visualized using a Schlieren-like representation define by $\log(1 + |\nabla \rho|)$:

Initially, the Mach 3 inflow impinges on the cylinder, generating a strong bow shock that propagates toward the upper and lower walls. Two oblique shocks form near the downstream

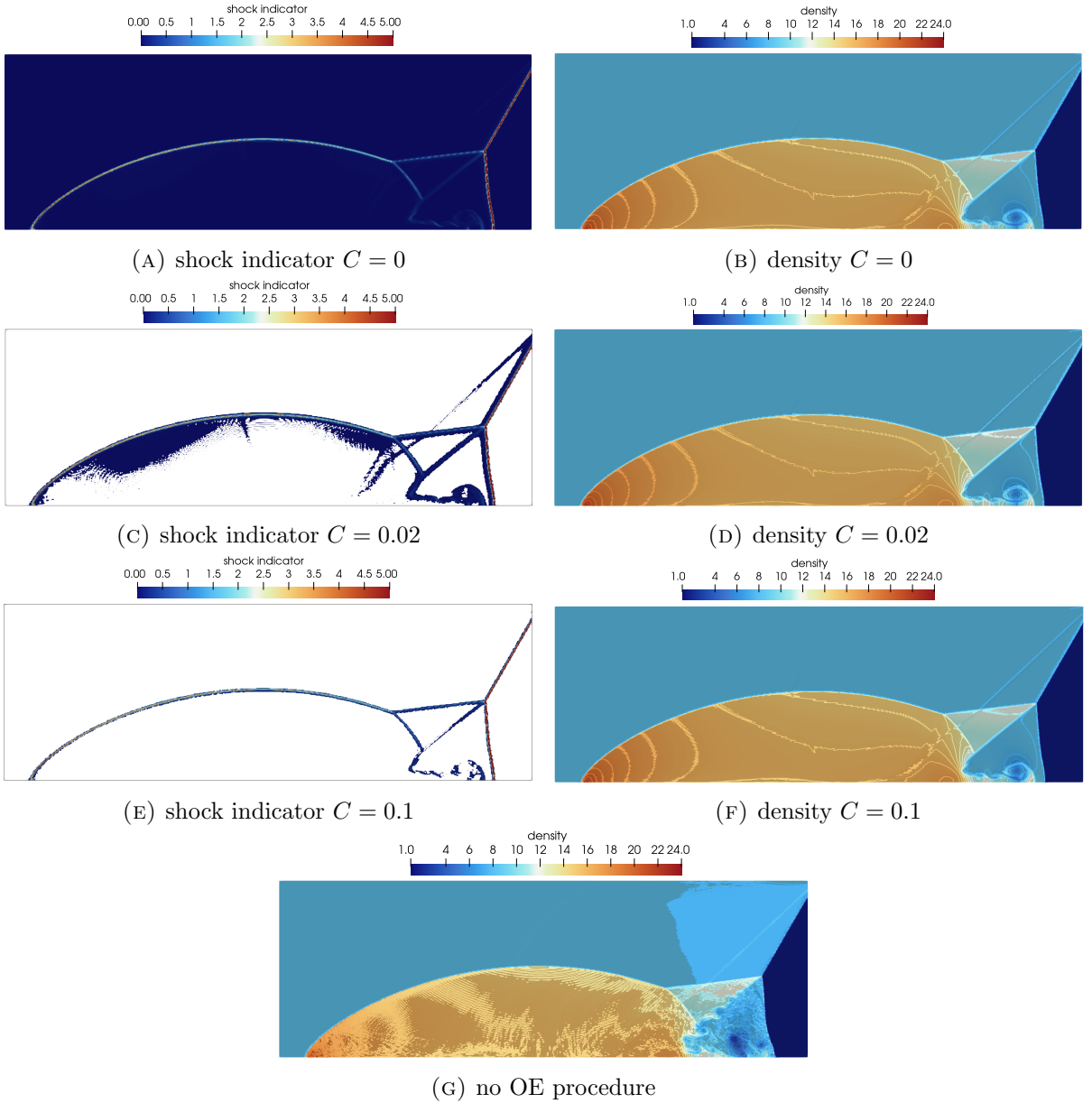


FIGURE 7. *Double Mach Reflection*: Shock indicator profile and density profile with different threshold value C .

sides of the cylinder and travel toward the outflow boundary. In addition, a distinct downstream shock, commonly referred to as the “fishtail” shock [16, 58], develops in the wake region. Flow separation occurs near the onset points of the oblique shocks, leading to a recirculating region behind the cylinder. Farther downstream, the wake becomes unsteady and a long trailing vortex structure emerges.

At later times ($t \gtrsim 2$), Kelvin–Helmholtz instabilities develop along the contact lines emanating from the shock-wave triple points near the upper and lower walls. The successful resolution of these small-scale roll-up structures indicates that the numerical diffusion introduced by the OE procedure remains sufficiently low. Overall, the computed flow structures are in good agreement with the results reported by Guermond et al. [36] and Deng [21]. The shock indicator distributions, shown in the right column of Figure 8, are well aligned with the locations of strong shocks, confirming that the OE procedure is selectively activated in nonsmooth regions.

We next compare solutions obtained with two different values of s . Figure 9 presents representative results for $s = 0.1$ and $s = 0.8$.

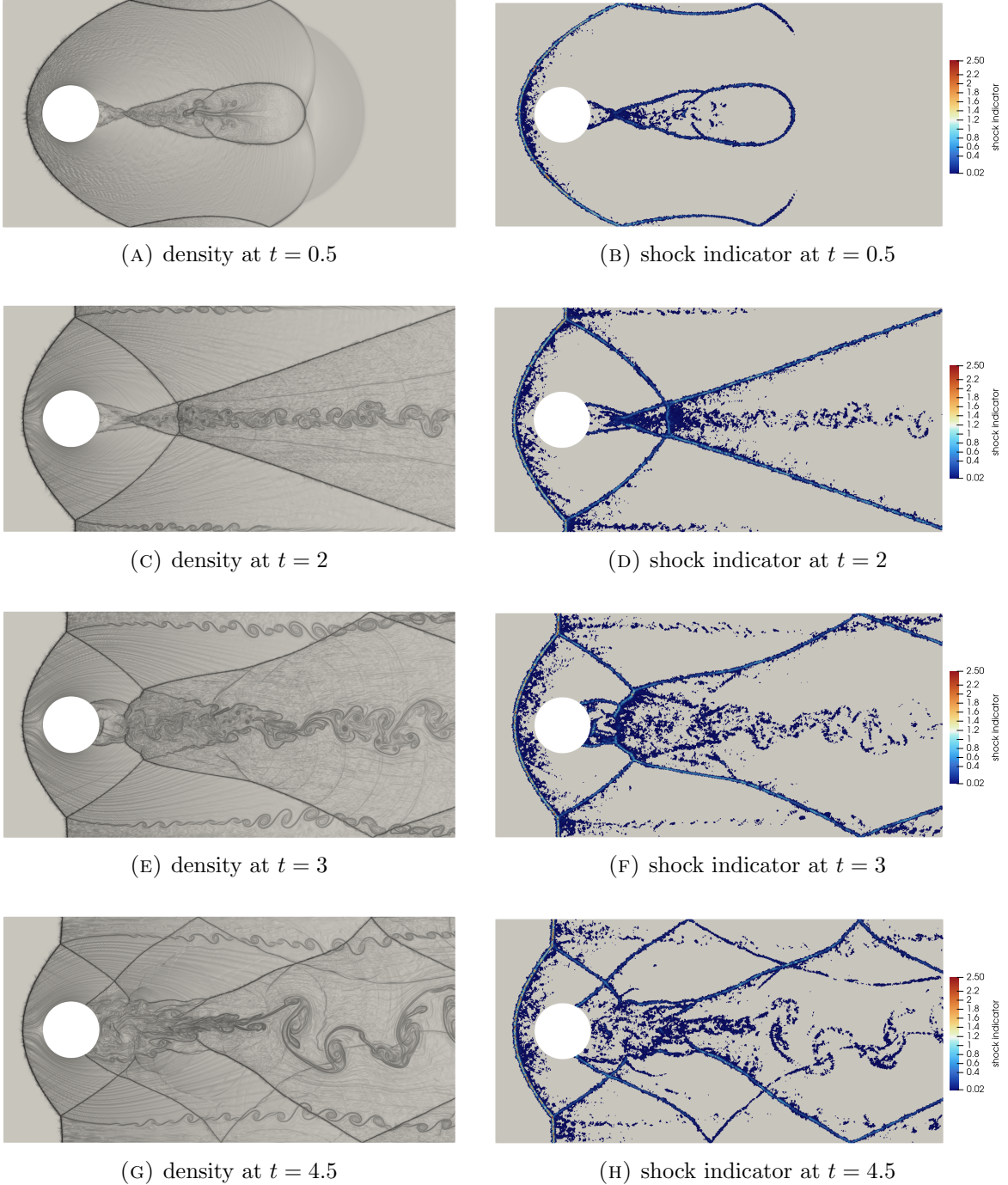


FIGURE 8. *Supersonic Flow Around a Two-Dimensional Cylinder*: the figures on the left row are Schlieren-like plot of density field; the figures on the right row are the distributions of shock indicator(73).

As shown in Figure 9, increasing the OE scaling factor leads to a noticeable increase in numerical dissipation. In particular, for $s = 0.8$, the Kelvin–Helmholtz instabilities developing along the contact lines near the upper and lower walls are significantly suppressed, indicating excessive numerical diffusion. In contrast, for the smaller value $s = 0.1$, these instabilities are well resolved, demonstrating that the OE procedure remains sufficiently non-dissipative to capture fine-scale flow features.

On the other hand, in the vicinity of the bow shock ahead of the cylinder, the case $s = 0.1$ exhibits more pronounced numerical oscillations, whereas these oscillations are strongly damped when $s = 0.8$. As a result of the different levels of numerical diffusion, the overall temporal

evolution of the flow differs between the two cases, although the main shock structures remain qualitatively similar. Similar sensitivity to numerical dissipation has been reported in [16], where variations in grid resolution and numerical schemes lead to noticeable differences in small-scale flow details, while the overall flow topology is preserved.

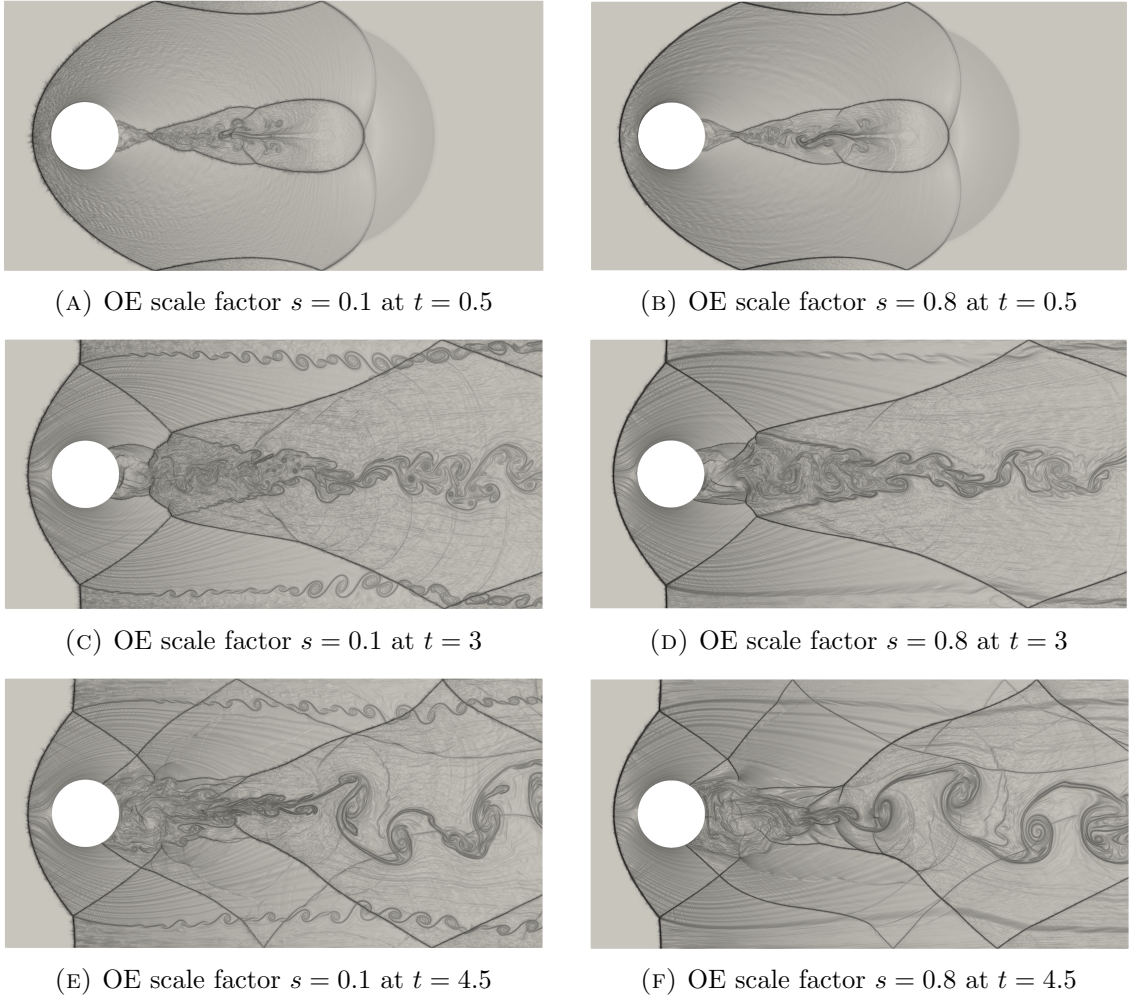


FIGURE 9. *Supersonic Flow Around a Two-Dimensional Cylinder*: the figures on the left row are computed with OE scale factor $s = 0.1$; the figures on the right row are computed with OE scale factor $s = 0.8$.

5.5. Explosion in a Domain with Multiple Cylinders. We next consider an explosion problem in a domain containing multiple cylindrical obstacles, which serves as a demanding benchmark for assessing the robustness of numerical schemes on complex geometries. Similar configurations have been studied in [58, 51, 70].

The computational domain is a two-dimensional circular region of radius 2 centered at the origin. Eight circular cylinders of radius 0.3 are placed inside the domain, with their centers located at a distance 1.4 from the origin and uniformly distributed at angular positions

$$\theta_k = \frac{k\pi}{4}, \quad k = 0, \dots, 7.$$

The mesh consists of second-order curvilinear quadrilateral elements generated using **Gmsh**, with a characteristic mesh size $h = 0.005$. The total number of elements is 215,805 with order 2.

The initial condition corresponds to a circular explosion. Inside a disk of radius $\sqrt{0.4}$ centered at the origin, the gas is set to $\rho = 1$, $p = 1$, and $\mathbf{u} = (0, 0)$. Outside this disk, the gas is initialized with $\rho = 0.125$, $p = 0.1$, and $\mathbf{u} = (0, 0)$. Reflective wall boundary conditions are imposed on all boundaries, including the outer circular boundary and the surfaces of the eight interior

cylinders. We use \mathbb{Q}_2 for the DG polynomial space, and set parameter $s = 0.8$ and $C = 0.02$ in this test.

Figure 10 presents Schlieren-type visualizations of the density field at several representative times. Initially, a strong circular shock is generated at the interface between the two gases and propagates radially outward. A circular contact discontinuity follows the shock at a slower speed, while a rarefaction wave travels inward toward the origin.

As the outward-propagating shock interacts with the cylindrical obstacles, part of the wave is reflected by the cylinder surfaces, while the remaining portion passes through the gaps between cylinders and subsequently impinges on the outer circular boundary. After reflection from the outer boundary, the shock wave propagates back toward the center of the domain. Meanwhile, the circular contact discontinuity weakens as it expands, eventually reverses direction, and moves inward. This contact interface becomes unstable and breaks down into small-scale vortical structures.

Overall, the computed flow evolution and wave interactions are in good agreement with previously reported results [58].

6. CONCLUDING REMARKS

In this work, we have developed an entropy-stable high-order nodal discontinuous Galerkin method for the two-dimensional compressible Euler equations on general curvilinear meshes, equipped with an improved oscillation-eliminating (OE) procedure. The formulation is built upon an entropy-stable DG spectral element method (DGSEM) that satisfies the summation-by-parts (SBP) property and discrete metric identities, entropy stability at the semidiscrete level on curvilinear grids.

To effectively control nonphysical oscillations near strong discontinuities, we incorporated a modified oscillation-eliminating discontinuous Galerkin (OEDG) procedure into the entropy-stable DG framework. Several improvements to the original OEDG method were introduced. First, an OE scaling factor was incorporated to regulate the strength of numerical damping, providing flexibility in balancing oscillation control and numerical dissipation. Second, we observed that the OE damping coefficients naturally serve as effective shock indicators. By localizing the OE procedure to troubled cells, the overall computational cost was significantly reduced. Third, the OE procedure was reformulated using projection operators, allowing for a systematic extension to curvilinear meshes, where local orthogonal modal bases are not readily available.

A comprehensive set of numerical experiments was presented to assess the accuracy, robustness, and effectiveness of the proposed method. The isentropic Euler vortex problem, which admits an exact analytical solution, was computed on curvilinear meshes, demonstrating that the method retains high-order accuracy and preserves entropy stability in the presence of geometric deformation. Two-dimensional Riemann problems were used to verify the ability of the method to accurately capture shocks, contact discontinuities, and complex wave interactions, with results consistent with those reported in the literature. The double Mach reflection problem further confirmed the robustness of the scheme in resolving strong shock interactions and intricate flow structures in the downstream region. We also compare the computation cost with different shock indicator threshold in double Mach reflection problem and found that the shock indicator can indeed improve the efficiency.

Particular emphasis was placed on challenging problems involving complex geometries. In the simulation of supersonic flow around a two-dimensional circular cylinder, the proposed method successfully resolved a wide range of flow features, including bow shocks, oblique shocks, contact discontinuities, fishtail shocks, and Kelvin–Helmholtz instabilities. A detailed comparison of different OE scaling factors revealed the expected trade-off between numerical dissipation and resolution of fine-scale flow features: larger scaling factors suppress small-scale instabilities, while smaller values preserve detailed structures at the expense of increased oscillations near strong shocks. Finally, the explosion problem in a domain with multiple cylinders further

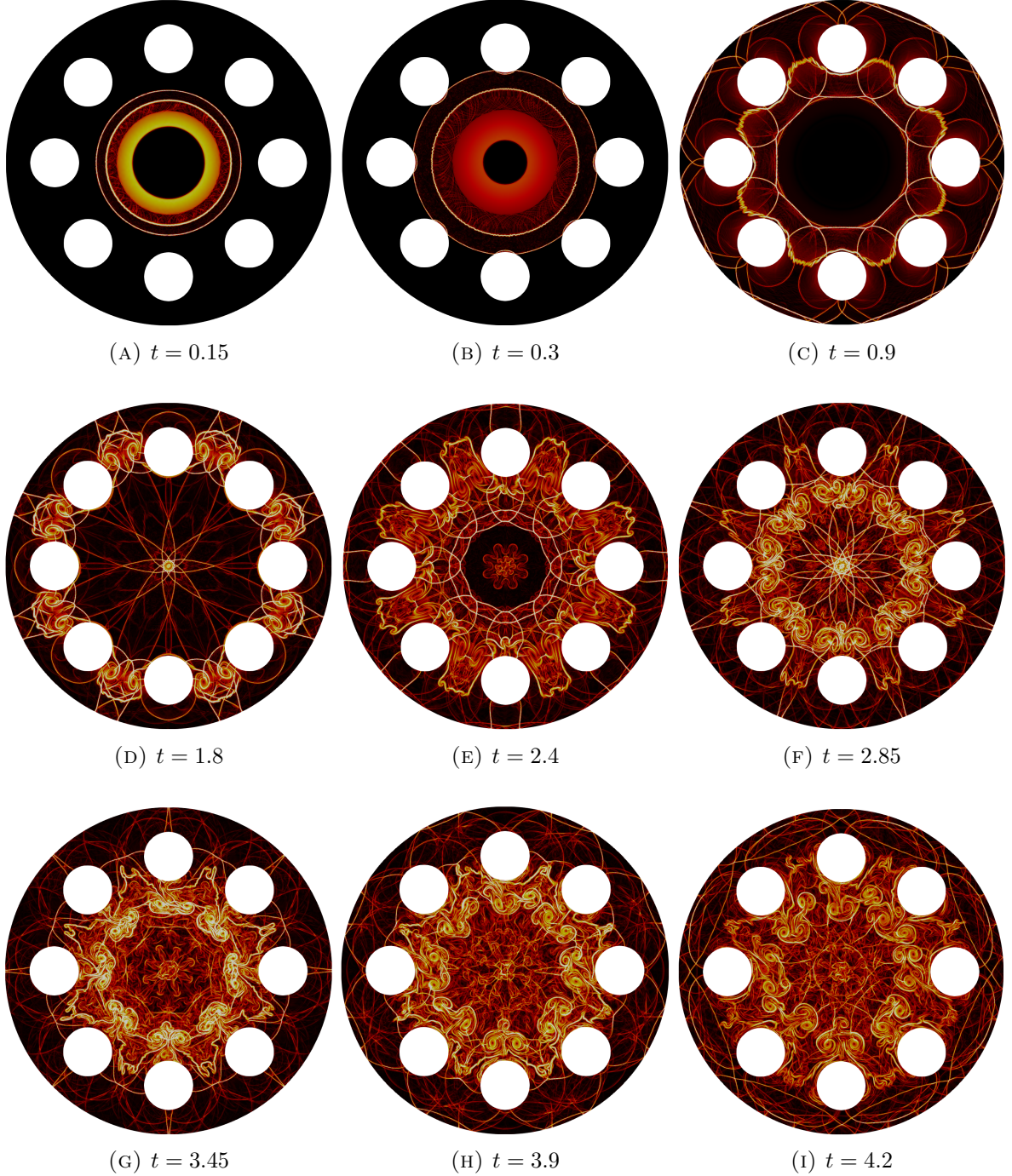


FIGURE 10. *Explosion in a Domain with Multiple Cylinders:* Schlieren diagram of the density at different time.

demonstrated the capability of the method to robustly and accurately capture complex shock dynamics in highly nontrivial curvilinear geometries.

Overall, the numerical results indicate that the proposed entropy-stable DGSEM combined with the modified OEDG procedure provides a robust and accurate framework for simulating compressible flows with strong discontinuities on general curvilinear meshes. The flexibility of the OE mechanism, together with entropy stability and high-order accuracy, makes the method a promising tool for challenging compressible flow applications involving complex geometries and multiscale flow phenomena. Future work will focus on extending the present entropy-stable OEDG framework to more complex systems, including the compressible Navier–Stokes equations

and magnetohydrodynamics. Such extensions would further demonstrate the versatility of the proposed approach for challenging flow problems on general curvilinear meshes.

APPENDIX: PROOF OF LEMMA 3.1

Proof. For notational simplicity, the element superscript $(\cdot)^e$ is omitted throughout this appendix.

The conservation property follows directly by summing the semidiscrete scheme (46) over all nodal indices p_1 and p_2 . Using the symmetry of the numerical fluxes and cancellation of interior contributions across element interfaces, one obtains exact conservation of all conserved variables (47).

The proof of entropy stability (48) is more involved, particularly in the presence of curvilinear coordinates. We multiply the semidiscrete scheme (46) by the entropy variables $(V_k)_{p_1, p_2}$ and sum over all nodal indices and equation components. After regrouping terms, this yields

$$\begin{aligned}
 0 = & \sum_{p_1=0}^N \sum_{p_2=0}^N \sum_{k=1}^4 w_{p_1} w_{p_2} \mathcal{J}_{p_1, p_2} (\partial_t U_k)_{p_1, p_2} (V_k)_{p_1, p_2} \\
 & + 2 \sum_{p_1=0}^N \sum_{p_2=0}^N \sum_{i=0}^N \sum_{k=1}^4 w_{p_1} w_{p_2} D_{p_1, i} (\tilde{f}_k^\#)_{(i, p_1), p_2} (V_k)_{p_1, p_2} \\
 (85) \quad & + 2 \sum_{p_1=0}^N \sum_{p_2=0}^N \sum_{j=0}^N \sum_{k=1}^4 w_{p_1} w_{p_2} D_{p_2, j} (\tilde{g}_k^\#)_{p_1, (j, p_2)} (V_k)_{p_1, p_2} \\
 & - \sum_{p_1=0}^N \sum_{k=1}^4 w_{p_1} \left(-(\tilde{g}_k - \tilde{g}_k^*)_{p_1, 0} (V_k)_{p_1, 0} + (\tilde{g}_k - \tilde{g}_k^*)_{p_1, N} (V_k)_{p_1, N} \right) \\
 & - \sum_{p_2=0}^N \sum_{k=1}^4 w_{p_2} \left(-(\tilde{f}_k - \tilde{f}_k^*)_{0, p_2} (V_k)_{0, p_2} + (\tilde{f}_k - \tilde{f}_k^*)_{N, p_2} (V_k)_{N, p_2} \right).
 \end{aligned}$$

For convenience, we decompose the above expression into four terms,

$$\begin{aligned}
 I &= \sum_{p_1=0}^N \sum_{p_2=0}^N \sum_{k=1}^4 w_{p_1} w_{p_2} \mathcal{J}_{p_1, p_2} (\partial_t U_k)_{p_1, p_2} (V_k)_{p_1, p_2}, \\
 II &= 2 \sum_{p_1=0}^N \sum_{p_2=0}^N \sum_{i=0}^N \sum_{k=1}^4 w_{p_1} w_{p_2} D_{p_1, i} (\tilde{f}_k^\#)_{(i, p_1), p_2} (V_k)_{p_1, p_2} \\
 & - \sum_{p_2=0}^N \sum_{k=1}^4 w_{p_2} \left(-(\tilde{f}_k)_{0, p_2} (V_k)_{0, p_2} + (\tilde{f}_k)_{N, p_2} (V_k)_{N, p_2} \right), \\
 III &= 2 \sum_{p_1=0}^N \sum_{p_2=0}^N \sum_{j=0}^N \sum_{k=1}^4 w_{p_1} w_{p_2} D_{p_2, j} (\tilde{g}_k^\#)_{p_1, (j, p_2)} (V_k)_{p_1, p_2} \\
 & - \sum_{p_1=0}^N \sum_{k=1}^4 w_{p_1} \left(-(\tilde{g}_k)_{p_1, 0} (V_k)_{p_1, 0} + (\tilde{g}_k)_{p_1, N} (V_k)_{p_1, N} \right), \\
 IV &= \sum_{p_1=0}^N \sum_{k=1}^4 w_{p_1} \left(-(\tilde{g}_k^*)_{p_1, 0} (V_k)_{p_1, 0} + (\tilde{g}_k^*)_{p_1, N} (V_k)_{p_1, N} \right) \\
 & + \sum_{p_2=0}^N \sum_{k=1}^4 w_{p_2} \left(-(\tilde{f}_k^*)_{0, p_2} (V_k)_{0, p_2} + (\tilde{f}_k^*)_{N, p_2} (V_k)_{N, p_2} \right).
 \end{aligned}$$

With this notation, (85) can be compactly written as

$$I + II + III + IV = 0.$$

We now simplify each term in turn. By definition of the entropy function $\eta(\mathbf{U})$, we have

$$\partial_t \eta = \sum_{k=1}^4 \frac{\partial \eta}{\partial U_k} \partial_t U_k = \sum_{k=1}^4 V_k \partial_t U_k.$$

Consequently, the first term can be written as

$$(86) \quad I = \sum_{p_1=0}^N \sum_{p_2=0}^N w_{p_1} w_{p_2} \mathcal{J}_{p_1, p_2} (\partial_t \eta)_{p_1, p_2},$$

which represents the discrete approximation of the time derivative of the cell entropy $\int_{\Omega_e} \eta \, dx$ using the LGL quadrature rule.

Next, we analyze the second term II . We fix the indices k and p_2 and consider the summation over p_1 and i . Define

$$II_{p_2, k} := 2 \sum_{p_1=0}^N \sum_{i=0}^N w_{p_1} D_{p_1, i} (\tilde{f}_k^\#)_{(i, p_1), p_2} (V_k)_{p_1, p_2} - \left(-(\tilde{f}_k)_{0, p_2} (V_k)_{0, p_2} + (\tilde{f}_k)_{N, p_2} (V_k)_{N, p_2} \right).$$

Using the symmetry of the entropy-conservative flux,

$$(\tilde{f}_k^\#)_{(i, p_1), p_2} = (\tilde{f}_k^\#)_{(p_1, i), p_2},$$

we obtain

$$\begin{aligned} II_{p_2, k} &= \sum_{p_1=0}^N \sum_{i=0}^N w_{p_1} D_{p_1, i} (\tilde{f}_k^\#)_{(i, p_1), p_2} (V_k)_{p_1, p_2} + \sum_{p_1=0}^N \sum_{i=0}^N w_i D_{i, p_1} (\tilde{f}_k^\#)_{(i, p_1), p_2} (V_k)_{i, p_2} \\ &\quad - \left(-(\tilde{f}_k)_{0, p_2} (V_k)_{0, p_2} + (\tilde{f}_k)_{N, p_2} (V_k)_{N, p_2} \right) \\ &= \sum_{p_1=0}^N \sum_{i=0}^N w_{p_1} D_{p_1, i} (\tilde{f}_k^\#)_{(i, p_1), p_2} \left((V_k)_{p_1, p_2} - (V_k)_{i, p_2} \right), \end{aligned}$$

where in the last step we used the SBP property (23) together with the consistency of the numerical flux,

$$(\tilde{f}_k^\#)_{(j, j), p_2} = (\tilde{f}_k)_{j, p_2}, \quad j = 0, N,$$

to cancel the boundary contributions.

Summing over all components $k = 1, \dots, 4$ and invoking the defining property of the entropy-conservative fluxes (39)–(44), we obtain

$$\sum_{k=1}^4 II_{p_2, k} = \sum_{p_1=0}^N \sum_{i=0}^N w_{p_1} D_{p_1, i} \left(\{\{y_\eta\}\}_{(i, p_1), p_2} (\psi_{p_1, p_2}^f - \psi_{i, p_2}^f) - \{\{x_\eta\}\}_{(i, p_1), p_2} (\psi_{p_1, p_2}^g - \psi_{i, p_2}^g) \right).$$

Using again the symmetry of the averaged metric terms,

$$\{\{y_\eta\}\}_{(i, p_1), p_2} = \{\{y_\eta\}\}_{(p_1, i), p_2}, \quad \{\{x_\eta\}\}_{(i, p_1), p_2} = \{\{x_\eta\}\}_{(p_1, i), p_2},$$

we have

$$\begin{aligned}
\sum_{k=1}^4 II_{p_2,k} &= \sum_{p_1=0}^N \sum_{i=0}^N (w_{p_1} D_{p_1,i} - w_i D_{i,p_1}) \left(\{y_\eta\}_{(i,p_1),p_2} \psi_{p_1,p_2}^f - \{x_\eta\}_{(i,p_1),p_2} \psi_{p_1,p_2}^g \right) \\
&= 2 \sum_{p_1=0}^N \sum_{i=0}^N w_{p_1} D_{p_1,i} \left(\{y_\eta\}_{(i,p_1),p_2} \psi_{p_1,p_2}^f - \{x_\eta\}_{(i,p_1),p_2} \psi_{p_1,p_2}^g \right) \\
&\quad - \underbrace{\left((y_\eta)_{N,p_2} \psi_{N,p_2}^f - (x_\eta)_{N,p_2} \psi_{N,p_2}^g \right)}_{=\tilde{\psi}_{N,p_2}^f} + \underbrace{\left((y_\eta)_{0,p_2} \psi_{0,p_2}^f - (x_\eta)_{0,p_2} \psi_{0,p_2}^g \right)}_{=\tilde{\psi}_{0,p_2}^f} \\
&= \sum_{p_1=0}^N \sum_{i=0}^N w_{p_1} D_{p_1,i} \left((y_\eta)_{i,p_2} \psi_{p_1,p_2}^f - (x_\eta)_{i,p_2} \psi_{p_1,p_2}^g \right) - \tilde{\psi}_{N,p_2}^f + \tilde{\psi}_{0,p_2}^f
\end{aligned}$$

where we used the SBP property (23) in the second equality, and the summation identity (24) in the last equality. This implies that

$$\begin{aligned}
II &= \sum_{p_2=0}^N w_{p_2} \sum_{k=1}^4 II_{p_2,k} = \sum_{p_2,p_1,i=0}^N w_{p_2} w_{p_1} D_{p_1,i} \left((y_\eta)_{i,p_2} \psi_{p_1,p_2}^f - (x_\eta)_{i,p_2} \psi_{p_1,p_2}^g \right) \\
(87) \quad &\quad + \sum_{p_2=0}^N w_{p_2} \left(-\tilde{\psi}_{N,p_2}^f + \tilde{\psi}_{0,p_2}^f \right).
\end{aligned}$$

Similar, we can simplify the third term to be

$$\begin{aligned}
III &= \sum_{p_1=0}^N \sum_{p_2=0}^N \sum_{j=0}^N w_{p_1} w_{p_2} D_{p_2,j} \left(- (y_\xi)_{p_1,j} \psi_{p_1,p_2}^f + (x_\xi)_{p_1,j} \psi_{p_1,p_2}^g \right) \\
(88) \quad &\quad + \sum_{p_1=0}^N w_{p_1} \left(-\tilde{\psi}_{p_1,N}^g + \tilde{\psi}_{p_1,0}^g \right).
\end{aligned}$$

Next, using the metric identity (25), there holds

$$\sum_{p_1=0}^N \sum_{p_2=0}^N \sum_{j=0}^N w_{p_1} w_{p_2} D_{p_2,j} (x_\xi)_{p_1,j} \psi_{p_1,p_2}^g = \sum_{p_2=0}^N \sum_{p_1=0}^N \sum_{i=0}^N w_{p_2} w_{p_1} D_{p_1,i} (x_\eta)_{i,p_2} \psi_{p_1,p_2}^g$$

and

$$\sum_{p_1=0}^N \sum_{p_2=0}^N \sum_{j=0}^N w_{p_1} w_{p_2} D_{p_2,j} (y_\xi)_{p_1,j} \psi_{p_1,p_2}^f = \sum_{p_2=0}^N \sum_{p_1=0}^N \sum_{i=0}^N w_{p_2} w_{p_1} D_{p_1,i} (y_\eta)_{i,p_2} \psi_{p_1,p_2}^f.$$

Hence the column integration terms in $II + III$ cancels out, and we are left with boundary contributions:

$$(89) \quad II + III = \sum_{p_2=0}^N w_{p_2} \left(-\tilde{\psi}_{N,p_2}^f + \tilde{\psi}_{0,p_2}^f \right) + \sum_{p_1=0}^N w_{p_1} \left(-\tilde{\psi}_{p_1,N}^g + \tilde{\psi}_{p_1,0}^g \right)$$

Finally, combining the above expression with IV , we get

$$\begin{aligned}
II + III + IV &= \sum_{p_1=0}^N \sum_{k=1}^4 w_{p_1} \left(-(\tilde{g}_k^*)_{p_1,0} (V_k)_{p_1,0} + \tilde{\psi}_{p_1,0}^g \right) + \sum_{p_1=0}^N \sum_{k=1}^4 w_{p_1} \left((\tilde{g}_k^*)_{p_1,N} (V_k)_{p_1,N} - \tilde{\psi}_{p_1,N}^g \right) \\
&\quad + \sum_{p_2=0}^N \sum_{k=1}^4 w_{p_2} \left(-(\tilde{f}_k^*)_{0,p_2} (V_k)_{0,p_2} + \tilde{\psi}_{0,p_2}^f \right) + \sum_{p_2=0}^N \sum_{k=1}^4 w_{p_2} \left((\tilde{f}_k^*)_{N,p_2} (V_k)_{N,p_2} - \tilde{\psi}_{N,p_2}^f \right)
\end{aligned}$$

Combining the above relation with (86), we conclude the proof of (48). \square

ACKNOWLEDGMENTS

Our numerical implementation is based on a DGSEM framework developed by Will Pazner within the MFEM library. We thank Will Pazner for kindly sharing his code with us and for valuable discussions related to the code design.

REFERENCES

- [1] Rémi Abgrall and Chi-Wang Shu, editors. *Handbook of Numerical Methods for Hyperbolic Problems: Applied and Modern Issues*, volume 18 of *Handbook of Numerical Analysis*. North Holland / Elsevier, Amsterdam, 2017.
- [2] Rémi Abgrall and Chi-Wang Shu, editors. *Handbook of Numerical Methods for Hyperbolic Problems: Basic and Fundamental Issues*. Handbook of Numerical Analysis, Vol. 17. North Holland / Elsevier, Amsterdam, 2016.
- [3] Robert Anderson, Julian Andrej, Andrew Barker, Jamie Bramwell, Jean-Sylvain Camier, Jakub Cerveny, Veselin Dobrev, Yohann Dudouit, Aaron Fisher, Tzanio Kolev, et al. Mfem: A modular finite element methods library. *Computers & Mathematics with Applications*, 81:42–74, 2021.
- [4] Julian Andrej, Nabil Atallah, Jan-Phillip Bäcker, Jean-Sylvain Camier, Dylan Copeland, Veselin Dobrev, Yohann Dudouit, Tobias Duswald, Brendan Keith, Dohyun Kim, et al. High-performance finite elements with mfem. *The International Journal of High Performance Computing Applications*, 38(5):447–467, 2024.
- [5] Garrett E Barter and David L Darmofal. Shock capturing with pde-based artificial viscosity for dgfem: Part i. formulation. *Journal of Computational Physics*, 229(5):1810–1827, 2010.
- [6] Marvin Bohm, Andrew R Winters, Gregor J Gassner, Dominik Derigs, Florian Hindenlang, and Joachim Saur. An entropy stable nodal discontinuous galerkin method for the resistive mhd equations. part i: Theory and numerical verification. *Journal of Computational Physics*, 422:108076, 2020.
- [7] Anne Burbeau, Pierre Sagaut, and Ch-H Bruneau. A problem-independent limiter for high-order runge–kutta discontinuous galerkin methods. *Journal of Computational Physics*, 169(1):111–150, 2001.
- [8] Mark H. Carpenter, Travis C. Fisher, Eric J. Nielsen, and Steven H. Frankel. Entropy stable spectral collocation schemes for the Navier-Stokes equations: discontinuous interfaces. *SIAM J. Sci. Comput.*, 36(5):B835–B867, 2014.
- [9] MH Carpenter, TC Fisher, EJ Nielsen, Matteo Parsani, M Svärd, and N Yamaleev. Entropy stable summation-by-parts formulations for compressible computational fluid dynamics. In *Handbook of Numerical Analysis*, volume 17, pages 495–524. Elsevier, 2016.
- [10] Jesse Chan. On discretely entropy conservative and entropy stable discontinuous galerkin methods. *Journal of Computational Physics*, 362:346–374, 2018.
- [11] Jesse Chan, David C Del Rey Fernández, and Mark H Carpenter. Efficient entropy stable gauss collocation methods. *SIAM Journal on Scientific Computing*, 41(5):A2938–A2966, 2019.
- [12] Jesse Chan and Lucas C Wilcox. On discretely entropy stable weight-adjusted discontinuous galerkin methods: curvilinear meshes. *Journal of Computational Physics*, 378:366–393, 2019.
- [13] Praveen Chandrashekar. Kinetic energy preserving and entropy stable finite volume schemes for compressible euler and navier-stokes equations. *Communications in Computational Physics*, 14(5):1252–1286, 2013.
- [14] Tianheng Chen and Chi-Wang Shu. Entropy stable high order discontinuous galerkin methods with suitable quadrature rules for hyperbolic conservation laws. *Journal of Computational Physics*, 345:427–461, 2017.
- [15] Tianheng Chen and Chi-Wang Shu. Review of entropy stable discontinuous galerkin methods for systems of conservation laws on unstructured simplex meshes. *CSIAM Transactions on Applied Mathematics*, 1(1):1–52, 2020.

- [16] Zeyu Chen and Kuangxu Chen. High-order positivity-preserving and dissipation-adaptive computational framework with sharp-interface immersed boundaries for high-mach-number shock-obstacle interactions. *Aerospace Science and Technology*, page 111073, 2025.
- [17] Bernardo Cockburn. Discontinuous galerkin methods for convection-dominated problems. In *High-order methods for computational physics*, pages 69–224. Springer, 1999.
- [18] Bernardo Cockburn and Chi-Wang Shu. Tvb runge-kutta local projection discontinuous galerkin finite element method for conservation laws. ii. general framework. *Mathematics of computation*, 52(186):411–435, 1989.
- [19] Jared Crean, Jason E Hicken, David C Del Rey Fernández, David W Zingg, and Mark H Carpenter. Entropy-stable summation-by-parts discretization of the euler equations on general curved elements. *Journal of Computational Physics*, 356:410–438, 2018.
- [20] David C Del Rey Fernández, Jason E Hicken, and David W Zingg. Simultaneous approximation terms for multi-dimensional summation-by-parts operators. *Journal of Scientific Computing*, 75(1):83–110, 2018.
- [21] Xi Deng. A new open-source library based on novel high-resolution structure-preserving convection schemes. *Journal of Computational Science*, 74:102150, 2023.
- [22] Shengrong Ding, Shumo Cui, and Kailiang Wu. Robust dg schemes on unstructured triangular meshes: Oscillation elimination and bound preservation via optimal convex decomposition. *Journal of Computational Physics*, 526:113769, 2025.
- [23] Jie Du, Yong Liu, and Yang Yang. An oscillation-free bound-preserving discontinuous galerkin method for multi-component chemically reacting flows. *Journal of Scientific Computing*, 95(3):90, 2023.
- [24] Travis C Fisher and Mark H Carpenter. High-order entropy stable finite difference schemes for nonlinear conservation laws: Finite domains. *Journal of Computational Physics*, 252:518–557, 2013.
- [25] Travis C. Fisher, Mark H. Carpenter, Jan Nordström, Nail K. Yamaleev, and Charles Swanson. Discretely conservative finite-difference formulations for nonlinear conservation laws in split form: Theory and boundary conditions. *Journal of Computational Physics*, 234(1):353–375, 2013.
- [26] Travis Calob Fisher. *High-order L2 stable multi-domain finite difference method for compressible flows*. PhD thesis, Purdue University, 2012.
- [27] Ulrik S Fjordholm, Siddhartha Mishra, and Eitan Tadmor. Arbitrarily high-order accurate entropy stable essentially nonoscillatory schemes for systems of conservation laws. *SIAM Journal on Numerical Analysis*, 50(2):544–573, 2012.
- [28] Lucas Friedrich, Andrew R. Winters, David C. Del Rey Fernández, Gregor J. Gassner, Matteo Parsani, and Mark H. Carpenter. An entropy stable h/p non-conforming discontinuous galerkin method with the summation-by-parts property. *Journal of Scientific Computing*, 77(2):689–725, 2018.
- [29] Guosheng Fu and Chi-Wang Shu. A new troubled-cell indicator for discontinuous galerkin methods for hyperbolic conservation laws. *Journal of Computational Physics*, 347:305–327, 2017.
- [30] Gregor J Gassner. A skew-symmetric discontinuous galerkin spectral element discretization and its relation to sbp-sat finite difference methods. *SIAM Journal on Scientific Computing*, 35(3):A1233–A1253, 2013.
- [31] Gregor J Gassner, Andrew R Winters, and David A Kopriva. Split form nodal discontinuous galerkin schemes with summation-by-parts property for the compressible euler equations. *Journal of Computational Physics*, 327:39–66, 2016.
- [32] Gregor J Gassner, Andrew R Winters, and David A Kopriva. A well balanced and entropy conservative discontinuous galerkin spectral element method for the shallow water equations. *Applied Mathematics and Computation*, 272:291–308, 2016.
- [33] Christophe Geuzaine and Jean-François Remacle. Gmsh: A 3-d finite element mesh generator with built-in pre-and post-processing facilities. *International journal for numerical methods in engineering*, 79(11):1309–1331, 2009.

- [34] David Gottlieb and Chi-Wang Shu. On the gibbs phenomenon and its resolution. *SIAM review*, 39(4):644–668, 1997.
- [35] Sigal Gottlieb, Chi-Wang Shu, and Eitan Tadmor. Strong stability-preserving high-order time discretization methods. *SIAM review*, 43(1):89–112, 2001.
- [36] Jean-Luc Guermond, Murtazo Nazarov, Bojan Popov, and Ignacio Tomas. Second-order invariant domain preserving approximation of the euler equations using convex limiting. *SIAM Journal on Scientific Computing*, 40(5):A3211–A3239, 2018.
- [37] Jean-Luc Guermond, Richard Pasquetti, and Bojan Popov. Entropy viscosity method for nonlinear conservation laws. *Journal of Computational Physics*, 230(11):4248–4267, 2011.
- [38] Jean-Luc Guermond and Bojan Popov. Fast estimation from above of the maximum wave speed in the Riemann problem for the Euler equations. *J. Comput. Phys.*, 321:908–926, 2016.
- [39] Amiram Harten. On the symmetric form of systems of conservation laws with entropy. *Journal of Computational Physics*, 49(1):151–164, 1983.
- [40] Songming Hou and Xu-Dong Liu. Solutions of multi-dimensional hyperbolic systems of conservation laws by square entropy condition satisfying discontinuous galerkin method. *Journal of Scientific Computing*, 31(1):127–151, 2007.
- [41] Thomas J. R. Hughes, Leopoldo P. Franca, and Michel Mallet. A new finite element formulation for computational fluid dynamics: I. symmetric forms of the compressible euler and navier–stokes equations and the second law of thermodynamics. *Computer Methods in Applied Mechanics and Engineering*, 54(2):223–234, 1986.
- [42] Farzad Ismail and Philip L Roe. Affordable, entropy-consistent euler flux functions ii: Entropy production at shocks. *Journal of Computational Physics*, 228(15):5410–5436, 2009.
- [43] Antony Jameson. Artificial diffusion, upwind biasing, limiters and their effect on accuracy and multigrid convergence in transonic and hypersonic flows. In *11th Computational Fluid Dynamics Conference*, page 3359, 1993.
- [44] Antony Jameson, Wolfgang Schmidt, and Eli Turkel. Numerical solution of the euler equations by finite volume methods using runge kutta time stepping schemes. In *14th fluid and plasma dynamics conference*, page 1259, 1981.
- [45] Guang Shan Jiang and Chi-Wang Shu. On a cell entropy inequality for discontinuous galerkin methods. *Mathematics of Computation*, 62(206):531–538, 1994.
- [46] David A. Kopriva. Metric identities and the discontinuous spectral element method on curvilinear meshes. *Journal of Scientific Computing*, 26(3):301–327, 2006.
- [47] Lilia Krivodonova, Jianguo Xin, J-F Remacle, Nicolas Chevaugeon, and Joseph E Flaherty. Shock detection and limiting with discontinuous galerkin methods for hyperbolic conservation laws. *Applied Numerical Mathematics*, 48(3-4):323–338, 2004.
- [48] Alexander Kurganov and Eitan Tadmor. Solution of two-dimensional riemann problems for gas dynamics without riemann problem solvers. *Numerical Methods for Partial Differential Equations: An International Journal*, 18(5):584–608, 2002.
- [49] Peter D Lax and Xu-Dong Liu. Solution of two-dimensional riemann problems of gas dynamics by positive schemes. *SIAM Journal on Scientific Computing*, 19(2):319–340, 1998.
- [50] Philippe G Lefloch, Jean-Marc Mercier, and Christian Rohde. Fully discrete, entropy conservative schemes of arbitrary order. *SIAM Journal on Numerical Analysis*, 40(5):1968–1992, 2002.
- [51] Richard Liska and Burton Wendroff. Comparison of several difference schemes on 1d and 2d test problems for the euler equations. *SIAM Journal on Scientific Computing*, 25(3):995–1017, 2003.
- [52] Mengqing Liu and Kailiang Wu. Structure-preserving oscillation-eliminating discontinuous galerkin schemes for ideal mhd equations: Locally divergence-free and positivity-preserving. *Journal of Computational Physics*, 527:113795, 2025.
- [53] Yong Liu, Jianfang Lu, and Chi-Wang Shu. An essentially oscillation-free discontinuous galerkin method for hyperbolic systems. *SIAM Journal on Scientific Computing*, 44(1):A230–A259, 2022.

- [54] Yong Liu, Jianfang Lu, and Chi-Wang Shu. An entropy stable essentially oscillation-free discontinuous galerkin method for hyperbolic conservation laws. *SIAM Journal on Scientific Computing*, 46(2):A1132–A1159, 2024.
- [55] Yong Liu, Jianfang Lu, and Chi-Wang Shu. An entropy stable essentially oscillation-free discontinuous galerkin method for solving ideal magnetohydrodynamic equations. *Journal of Computational Physics*, 530:113911, 2025.
- [56] Yong Liu, Jianfang Lu, Qi Tao, and Yinhua Xia. An oscillation-free discontinuous galerkin method for shallow water equations. *Journal of Scientific Computing*, 92(3):109, 2022.
- [57] Jianfang Lu, Yong Liu, and Chi-Wang Shu. An oscillation-free discontinuous galerkin method for scalar hyperbolic conservation laws. *SIAM Journal on Numerical Analysis*, 59(3):1299–1324, 2021.
- [58] Murtazo Nazarov and Aurélien Larcher. Numerical investigation of a viscous regularization of the euler equations by entropy viscosity. *Computer Methods in Applied Mechanics and Engineering*, 317:128–152, 2017.
- [59] Manting Peng, Zheng Sun, and Kailiang Wu. Oedg: Oscillation-eliminating discontinuous galerkin method for hyperbolic conservation laws. *Mathematics of Computation*, 94(353):1147–1198, 2025.
- [60] Per-Olof Persson and Jaime Peraire. Sub-cell shock capturing for discontinuous galerkin methods. In *44th AIAA aerospace sciences meeting and exhibit*, page 112, 2006.
- [61] Jianxian Qiu and Chi-Wang Shu. A comparison of troubled-cell indicators for runge–kutta discontinuous galerkin methods using weighted essentially nonoscillatory limiters. *SIAM Journal on Scientific Computing*, 27(3):995–1013, 2005.
- [62] Jianxian Qiu and Chi-Wang Shu. Runge–kutta discontinuous galerkin method using weno limiters. *SIAM Journal on Scientific Computing*, 26(3):907–929, 2005.
- [63] J-F Remacle, Jonathan Lambrechts, Bruno Seny, Emilie Marchandise, Amaury Johnen, and C Geuzainet. Blossom-quad: A non-uniform quadrilateral mesh generator using a minimum-cost perfect-matching algorithm. *International journal for numerical methods in engineering*, 89(9):1102–1119, 2012.
- [64] Florent Renac. Entropy stable dgsem for nonlinear hyperbolic systems in nonconservative form with application to two-phase flows. *Journal of Computational Physics*, 382:1–26, 2019.
- [65] Carsten W Schulz-Rinne, James P Collins, and Harland M Glaz. Numerical solution of the riemann problem for two-dimensional gas dynamics. *SIAM Journal on Scientific Computing*, 14(6):1394–1414, 1993.
- [66] Chi-Wang Shu. High-order finite difference and finite volume weno schemes and discontinuous galerkin methods for cfd. *International Journal of Computational fluid dynamics*, 17(2):107–118, 2003.
- [67] Chi-Wang Shu. Essentially non-oscillatory and weighted essentially non-oscillatory schemes for hyperbolic conservation laws. In *Advanced Numerical Approximation of Nonlinear Hyperbolic Equations: Lectures given at the 2nd Session of the Centro Internazionale Matematico Estivo (CIME) held in Cetraro, Italy, June 23–28, 1997*, pages 325–432. Springer, 2006.
- [68] Eitan Tadmor. The numerical viscosity of entropy stable schemes for systems of conservation laws. i. *Mathematics of Computation*, 49(179):91–103, 1987.
- [69] Eitan Tadmor. Entropy stability theory for difference approximations of nonlinear conservation laws and related time-dependent problems. *Acta Numerica*, 12:451–512, 2003.
- [70] Eleuterio F Toro. *Riemann solvers and numerical methods for fluid dynamics: a practical introduction*. Springer Science & Business Media, 2013.
- [71] Peter E Vincent, Patrice Castonguay, and Antony Jameson. Insights from von neumann analysis of high-order flux reconstruction schemes. *Journal of Computational Physics*, 230(22):8134–8154, 2011.
- [72] Lei Wei, Lingling Zhou, and Yinhua Xia. The jump filter in the discontinuous galerkin method for hyperbolic conservation laws. *Journal of Computational Physics*, 520:113498, 2025.

- [73] Niklas Wintermeyer, Andrew R Winters, Gregor J Gassner, and David A Kopriva. An entropy stable nodal discontinuous galerkin method for the two dimensional shallow water equations on unstructured curvilinear meshes with discontinuous bathymetry. *Journal of Computational Physics*, 340:200–242, 2017.
- [74] Paul Woodward and Phillip Colella. The numerical simulation of two-dimensional fluid flow with strong shocks. *Journal of computational physics*, 54(1):115–173, 1984.
- [75] Ruifang Yan, Remi Abgrall, and Kailiang Wu. Uniformly high-order bound-preserving oedg schemes for two-phase flows. *Mathematical Models and Methods in Applied Sciences*, 34(13):2537–2610, 2024.
- [76] Fengrui Zhang and Yulia T Peet. Discontinuous galerkin spectral element method for shock capturing with summation by parts properties. *Journal of Computational Physics: X*, 17:100123, 2023.
- [77] Xiangxiong Zhang. On positivity-preserving high order discontinuous galerkin schemes for compressible navier–stokes equations. *Journal of Computational Physics*, 328:301–343, 2017.
- [78] Xiangxiong Zhang and Chi-Wang Shu. On positivity-preserving high order discontinuous galerkin schemes for compressible euler equations on rectangular meshes. *Journal of Computational Physics*, 229(23):8918–8934, 2010.
- [79] Xinghui Zhong and Chi-Wang Shu. A simple weighted essentially nonoscillatory limiter for runge–kutta discontinuous galerkin methods. *Journal of Computational Physics*, 232(1):397–415, 2013.
- [80] Jun Zhu, Jianxian Qiu, Chi-Wang Shu, and Michael Dumbser. Runge–kutta discontinuous galerkin method using weno limiters ii: unstructured meshes. *Journal of Computational Physics*, 227(9):4330–4353, 2008.
- [81] Hujian Zuo, Weifeng Zhao, and Ping Lin. A positivity preserving and oscillation-free entropy stable discontinuous galerkin scheme for the reactive euler equations. *Journal of Computational Physics*, 505:112906, 2024.

¹ DEPARTMENT OF APPLIED AND COMPUTATIONAL MATHEMATICS AND STATISTICS (ACMS), UNIVERSITY OF NOTRE DAME, NOTRE DAME, IN 46556

Email address: jyang38@nd.edu, gfu@nd.edu